In situ measurement method for the quantification of the thermal transmittance of a non-homogeneous wall or a thermal bridge using an inverse technique and active infrared thermography

Adrien François, Laurent Ibos, Vincent Feuillet, Johann Meulemans

Energy & Buildings 233 (2021) 110633, https://doi.org/10.1016/j.enbuild.2020.110633

In situ measurement method for the quantification of the thermal transmittance of a non-homogeneous wall or a thermal bridge using an inverse technique and active infrared thermography

Adrien François*[1,2], Laurent Ibos[1], Vincent Feuillet[1], and Johann Meulemans[2]

[1]Université Paris-Est Créteil, CERTES, F-94010 Créteil, France
[2]Saint-Gobain Research Paris, 39 quai Lucien Lefranc, F-93303 Aubervilliers, France

August 28, 2020

Abstract

Thermal bridges tend to increase overall buildings energy demand and might cause water condensation problems. They are thermally characterized by a linear transmission coefficient ψ or a point transmission coefficient χ. Today, most studies of thermal bridges are based on theoretical or numerical calculations. Standardized methods define default values and assumptions to make in simple or detailed simulations. The few existing *in situ* characterization methods of thermal bridges are based on steady-state assumptions. This makes them highly sensitive to weather conditions and often requires very long measurements. The present paper proposes a novel active method for the *in situ* characterization of a thermal bridge. It generalizes a measurement of a homogeneous wall thermal resistance. The indoor air is rapidly heated for a few hours (typically 6) and the wall thermal response is analyzed with an inverse technique based on a white-box model. Surface temperatures and heat fluxes are measured with contact sensors on a sound area and these quantities are then extrapolated to nearby thermal bridges using infrared thermography. The total heat transfer coefficient, required in the heat flux extrapolation process, is monitored with a specific device. The method is validated on a full-size load-bearing wall built inside a climate chamber. The mechanical supports, holding the internal insulation system implemented on the wall, generate several thermal bridges. The ψ-values estimated by the active method are less than 20% away from steady-state measurements taken as reference. Many configurations were tested with constant and varying external temperature and the method proved its robustness to these unsteady conditions.

Keywords— *in situ*; measurements; thermal resistance; thermal bridges; building envelope; inverse methods; heat transfer coefficient; active infrared thermography; non-destructive testing (NDT)

*corresponding author: adrien.francois@u-pec.fr

Nomenclature

Acronyms

HFM	Heat Flux Meter
IRT	Infrared Thermography
MRT	Mean Radiant Temperature
ROI	Region Of Interest
SA	Sound Area
TB	Thermal Bridge
TEC	ThermoElectric Cooler

Greek Symbols

β	parameter vector	
ω	pulsation	$\mathrm{rad.s^{-1}}$
Φ	heat flux	W
ψ	thermal bridge transmission coefficient	$\mathrm{W.m^{-1}.K^{-1}}$
ρ	correlation coefficient	–
σ	measurement noise standard deviation	
σ_{SB}	Stefan-Boltzmann constant	$\mathrm{W.m^{-2}.K^{-4}}$
τ	atmosphere transmittance	–
ε	wall emissivity / white noise	–
φ	heat flux per unit surface	$\mathrm{W.m^{-2}}$
ζ	phase lag	rad

Roman Symbols

$\mathcal{A}$	Amplitude	
A, B, C, D	thermal quadrupole coefficients	
b	thermal effusivity	$\mathrm{J.K^{-1}.m^{-2}.s^{-1/2}}$
f	frequency	$\mathrm{s^{-1}}$
FT	Fourier Transform	
h	heat transfer coefficent	$\mathrm{W.m^{-2}.K^{-1}}$
I	radiative intensity	$\mathrm{W.m^{-2}.sr^{-1}.nm^{-1}}$
I°	Planck radiative intensity	$\mathrm{W.m^{-2}.sr^{-1}.nm^{-1}}$
J	Cost function	
L_z	thermal bridge length	m
L_{tb}	thermal bridge width	m
n_L	wall number of layers	
p	Laplace variable	$\mathrm{s^{-1}}$
R	thermal resistance	$\mathrm{m^2.K.W^{-1}}$
T	temperature	K
U	wall thermal transmittance	$\mathrm{W.m^{-2}.K^{-1}}$
X^*	reduced sensitivity coefficient	
u	uncertainty	

Superscripts

–	mean quantity (space average)
$\sim$	Laplace transform
$\wedge$	estimated value
app	apparent
c	convective
r	radiative

Subscripts

–	complex harmonic quantity
1D	One Dimensional (sound area)
air	air / atmosphere
e	external
env	environment
i	internal
in	interface glass wool/building blocks
insul	insulation system
mo	model
op	operative
s	surface of the wall
tb	thermal bridge

1 Introduction

In the aim of limiting the effects of global warming, several targets were set by the European Union (EU) 2030 climate & energy framework. They focus on reducing greenhouse gas emissions, increasing the share for renewable energy, and improving energy efficiency of systems. The building sector has a major role to play to reach these goals. Indeed, 40% of total energy consumption in the EU is attributable to residential and non-residential buildings [1].

The assessment of the energy performance of a building usually relies on theoretical calculations. When the output of these calculations is compared to *in situ* measurements, the actual energy performance often shows some discrepancy. This is the so-called "performance gap" (see [2, 3, 4, 5] and references therein). It may be due to several factors such as aging, quality of construction, but also thermal bridging. In order to address the issues behind the performance gap, the overall energy performance of a building is not enough. The contribution of each element of the envelope (walls, openings, roof and floor) to the whole heat loss coefficient (HLC) has to be determined.

Multi-layer walls with high thermal resistance are widely used to reduce heat losses in buildings. Nevertheless, the presence of thermal bridges tends to reduce their performance by increasing winter heat losses and summer heat gains [6]. Depending on the building, thermal bridges can represent 11 % to 30 % of the energy final demand [7]. In cold climates, not only do thermal bridges impact the thermal comfort of occupants, they also increase the risk of condensation and mould growth [8] [9]. This may damage the building envelope and cause sanitary issues. Two main types of thermal bridges can be found in a building [6]. "Geometrical" or "structural" thermal bridges are due to the overall shape of the building (e.g. wall/floor junctions, corners) whereas "material-related" ones are induced by irregularities in the insulation layers (e.g. mechanical supports of insulating materials).

A homogeneous wall is thermally characterized by a thermal transmittance U $\left(\mathrm{W.m^{-2}.K^{-1}}\right)$. Similarly, linear thermal bridges are characterized by linear a thermal transmittance ψ $\left(\mathrm{W.m^{-1}.K^{-1}}\right)$ and point thermal bridges by a point thermal transmittance χ $\left(\mathrm{W.K^{-1}}\right)$:

$$\psi = \frac{\phi_{\mathrm{tb}}}{L_{\mathrm{z}} \times \Delta T_{\mathrm{ie}}} \tag{1}$$

$$\chi = \frac{\phi_{\mathrm{tb}}}{\Delta T_{\mathrm{ie}}} \tag{2}$$

with ΔT_{ie} the internal/external temperature difference, L_{z} the linear thermal bridge length, and ϕ_{tb} the additional heat flux attributable to the thermal bridge, as illustrated in Fig 1.

The ψ and χ coefficients may also be expressed as:

$$\psi = L_{\mathrm{tb}} \left(U_{\mathrm{tb}} - U_{\mathrm{1D}}\right) \tag{3}$$

$$\chi = A_{\mathrm{tb}} \left(U_{\mathrm{tb}} - U_{\mathrm{1D}}\right) \tag{4}$$

with U_{tb} the transmittance of the wall with its thermal bridge, U_{1D} the transmittance of the same wall without it, L_{tb} the width of a linear thermal bridge and A_{tb} the area of the point thermal bridge.

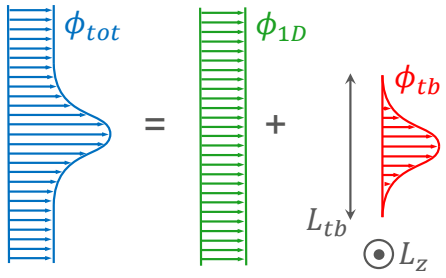

Figure 1: Illustration of additional heat flux induced by a thermal bridge.

Today, there is no standardized method for the *in situ* characterization of thermal bridges. Existing studies mainly deal with theoretical and numerical works in which strong assumptions are made. Standardized approaches are based either on default/design values [10, 6], simplified calculations (ISO 14683 [11]) or detailed calculations (ISO 10211 [12]). These methods assume that the wall stratigraphy is perfectly known and rely on default values for the thermal properties of the materials and both the external and internal environments (air temperature, relative humidity, wind, etc.). Therefore, they may lead to a preliminary assessment of the building envelope but they generally do not have a good accordance with the results of actual operating conditions [9].

Experimental studies on thermal bridges are quite limited in literature because they are tedious, expensive and time-consuming [9]. The few existing *in situ* measurement methods are based on steady-state assumptions. Because such a state is seldomly reached in a building, the results may be very sensitive to weather conditions and sometimes require very long measurements.

This work proposes a novel dynamic method for the *in situ* characterization of thermal bridges. It is a generalization of a technique developed by the authors for the measurement of a homogeneous wall thermal resistance [13]. It mainly consists in heating the indoor air and using inverse methods to estimate the wall thermal resistance from heat flux and temperature measurements. The method only requires a few hours of measurements (typically 6). By measuring the surface temperature and heat flux fields on the thermal bridge, this same inverse technique may be applied to estimate the equivalent thermal resistance of a non-homogeneous wall. The temperature and heat flux are extrapolated from a sound area to the thermal bridge using infrared thermography (IRT) and a device to estimate the global surface heat transfer coefficient [14]. The method is validated on a full-scale wall built inside a climate chamber. The layout of this wall (a load bearing wall supplemented by an internal insulation system) is commonly found in the French building stock. The irregularities in the insulation system (due to the presence of metallic rails used to hold the insulating materials) form material-related thermal bridges.

Section 2 of this paper presents a state of the art of qualitative and quantitative methods for the assessment of thermal bridges in buildings. Section 3 introduces the studied wall and the experimental campaign conducted. Sections 4 and 5 respectively present the steady-state and active (or dynamic)

methods used for the quantification of thermal bridge transmission coefficients. Finally, the results of each approach are detailed in sections 4.2 and 6.

2 State of the art

Many qualitative studies focus on the detection of thermal bridges. ISO standard 13187 [15] specifies a method, by thermographic examination, for detecting thermal irregularities in building envelopes. The use of IRT for building applications was extensively documented in the past decades (e.g., see [16, 17, 18, 19] and references therein). Several recent studies [20, 21] deal with the automatic detection of thermal bridges from infrared images.

Two approaches are possible for the use of infrared thermography in buildings, namely "active" and "passive". With passive IRT, the building is observed under natural conditions when the indoor/outdoor temperature gradient is high enough for thermal irregularities to be detectable. This is the most commonly used approach. With active IRT however, the building is subject to a thermal load and its dynamic response is analyzed. This is a common practice in the field of thermal non-destructive testing (NDT) of materials. Active IRT in the building sector was first introduced by Grinzato [22]. The thermal load may be for instance an artificial radiant heater [23, 24, 25] or the sun [26, 27, 28, 29, 30]. Douguet *et al.* [31] also developed a thermal bridge detection technique based on heating of the indoor air. This method has the advantage of being applicable regardless of the season and the weather conditions.

Yet, as stated above, most quantitative studies dealing with thermal bridges are theoretical. Standardized approaches propose design/default values [10, 6], or calculations: ISO 14683 [11]. This standard presents simplified calculation methods for the assessment of thermal bridges as well as a catalog of default thermal transmittances. ISO 10211 [12] sets out the specifications for a three-dimensional and a two-dimensional geometrical model of a thermal bridge for the numerical calculation of heat fluxes, minimum surface temperatures and thermal transmittances. In addition, some efforts were made in the literature to develop equivalent wall models of thermal bridges in order to include them easily in building energy simulation softwares [32, 33, 34, 35, 36, 37, 38]. Some studies also combine measurements and calculations to assess thermal performances of a building façade [25, 39, 40, 41] or for the validation of a thermal modeling [42, 43, 44, 45, 46, 47]. Nevertheless, these calculation-based approaches often relies on strong assumptions.

Several authors performed quantitative experimental studies of thermal bridges using a hot box test facility. Martin *et al.* [48] studied the impact of a reinforced concrete pillar in a brick wall. They performed steady-state measurements (following recommendations from ISO 8990 [49]) as well as dynamic tests in which the room temperature followed a sinusoidal variation. O'Grady *et al.* [50, 51] studied several samples in indoor and outdoor configurations. Thermal bridge transmission coefficients are quantified in steady-state. The method used, based on the calculation of "incidence factors" with infrared thermography, was introduced by Asdrubali *et al.* [52]. The incidence factor is the ratio of the wall transmittance with and without the thermal bridge:

$$I_{\mathrm{tb}} = \frac{U_{\mathrm{tb}}}{U_{\mathrm{1D}}} \tag{5}$$

Baldinelli *et al.* [53] used the same approach coupled with a mathematical algorithm to enhance the thermal image resolution. The temperature factor f_{Rsi} is also a dimensionless number used for thermal bridges. It is useful to evaluate the risk of mould growth on thermal bridges [39]:

$$f_{\mathrm{Rsi}} = \frac{T_{\mathrm{si}} - T_{\mathrm{e}}}{T_{\mathrm{i}} - T_{\mathrm{e}}} \tag{6}$$

with T_{si} the internal surface temperature, T_{e} the external temperature and T_{i} the internal temperature. To avoid mould growth, the surface temperature factor should be above a critical which depends on the building type and country [54].

The *in situ* characterization of thermal bridges is more complex because the environment is not controlled as it is inside a guarded hot box. Benko [55] is one of the first to have used infrared thermography for the quantitative assessment of thermal bridges. He focuses on wall-joints on the façade of a multi-storey building and introduces the dimensionless energy saving factor. The latter is the ratio of the heat flux through the building wall with and without thermal bridge. Asdrubali *et al.* [52] further developed the concept and renamed this ratio the "Incidence factor" (or "impact factor"). The thermal bridge transmittance may be calculated from this factor. The method is tested on an experimental test cell under quasi-steady-state conditions. In Bianchi *et al.* [56], the same authors, applied the incidence factor technique on an outdoor test room. Thermal bridges investigated are vertical lines between walls, and horizontal lines between walls and roof/floor. The accuracy of the method was improved by the application of mathematical algorithm to enhance thermal image resolution [20]. Nardi *et al.* [57] studied the effect of three different thermal bridges in a house (edges between walls and roof) under several climatic conditions. Finally, the uncertainty over the measurement of the incidence factor were reduced by the authors in [58].

This literature review showed that the tools available for the *in situ* quantitative assessment of thermal bridges are still limited today. Many studies focused on the qualitative detection of thermal bridges using infrared thermography, sometimes with an active approach. However, most quantitative studies on this topic are theoretical: the only existing standards are base on default values and numerical simulations. The few existing *in situ* thermal bridge characterization methods are based on steady-state assumptions. This makes the measurement methods highly dependent on the weather conditions and difficult to apply *in situ*. To overcome these limitations, the present study proposes an active method for the *in situ* characterization of a thermal bridge (or more generally a non-homogeneous wall). Thanks to the use of an artificial thermal load, the method is not limited to winter-time measurements and is less sensitive to unsteady outdoor temperatures.

3 Experimental setup

3.1 Wall and climate chamber

The measurement method was tested on a full-size load bearing wall built inside a $4 \times 4 \times 3$ m^3 climate chamber at

CEREMA, Nancy (France). As shown in Fig 2, the chamber contains two independent modules able to control the air temperature between −30 and +30°C. The wall is built between them so that a different temperature may be set on each side. The design temperatures may be constant or variable.

Figure 2: Photography of the two modules inside the climate chamber before the construction of the wall.

The studied wall is 3.3 m wide and 2 m high. It is a load bearing wall made out of 200 mm thick concrete building blocks on witch a standard internal insulation system is fixed. This is a common configuration of French buildings. The insulation layer is made of 100 mm of glass wool hold with metallic rails. Gypsum boards are then fixed on these rails and the joints between them are made. Figure 3 shows a picture of the wall before the installation of the gypsum boards. A thin door is placed on the right-hand side.

Figure 3: Photography of the wall before installation of the gypsum boards.

Metallic rails of different geometries were used in order to generate several types of thermal bridges. A cut-out of the wall is presented in Fig 4. The first two thermal bridges, noted “TB 1” and “TB 2”, are made of 48 mm thick metallic rails (these rails therefore crosses about half of the insulation layer). The difference between them is that TB 1 is located in the middle of a gypsum board whereas TB 2 falls at the junction between two boards. In addition, there is no screw on TB 1. The metallic rails used for the third thermal bridge, referred as “TB 3”, are 100 mm thick: they completely go through the glass wool layer. Finally, there is a 1.2 m wide zone free from thermal bridge in the middle of the wall. On this “sound area” (SA), the surface temperature is uniform so that heat transfers are one dimensional (1D).

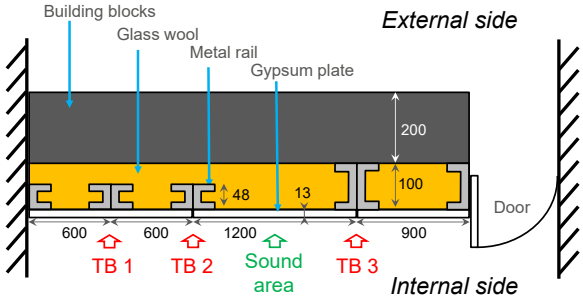

Figure 4: Illustration of wall layout and position of the thermal bridges (dimensions in mm).

3.2 Contact measurements

Several contact sensors are implemented on the studied wall. Temperatures are measured with T-type thermocouples. The air temperature is measureThe authors do not anticipate any difficulty to apply the same methods to lightweight wallsd in the center of the room by thermocouples shielded from radiation with aluminum tape. A platinum sensor was used to calibrate the thermocouples between 0 and 50°C. It was used with an AOIP TM6612 temperature datalogger. The measurement uncertainty of this reference is 0.2°C. An external calibration of these devices was performed in order to ensure the metrological traceability to the ITS-90 [59]. In addition, heat flux meters from Captec© monitor surface heat fluxes. They are 100×100 mm² large, have a 0.54 mm thickness and a sensitivity above $60\,\mu V.(W.m^{-2})^{-1}$ given with a 3 % uncertainty. For the HFMs to be as less intrusive as possible, they were covered with adhesive tape that have similar optical properties as the wall surface: same emissivity (0.94 in the 2-20 µm band) and diffuse reflection[1]. Temperatures and heat fluxes are recorded every 3 s and averaged every 5 points. The sensors are plugged on National Instruments© NI9214 conditioning modules. These modules communicate with a PC computer via a 8-slot NI CompactDAQ USB chassis. The experimental setup is monitored by a LabView© application.

The location of the main sensors are indicated in Fig 5.

3.3 Infrared thermography

An infrared camera (reference SC7000 from FLIR©) was used to monitor surface temperature differences. It has a cooled matrix sensor of 320×256 pixels working in the $7.7 - 9.2$ µm spectral band and has a 20 mK sensitivity. Each recorded image is an average of 200 frames taken within 2 s.

[1] The emissivities were measured with an infrared spectrometer (Frontier model, from Perkin-Elmer©) equipped with an integrating sphere (from Pike©). A diffusing gold surface (SpectraGold©) was used as reference and its reflectance was measured by an independent method at the French National Metrology Institute (LNE: Laboratoire National de métrologie et d’Essais).

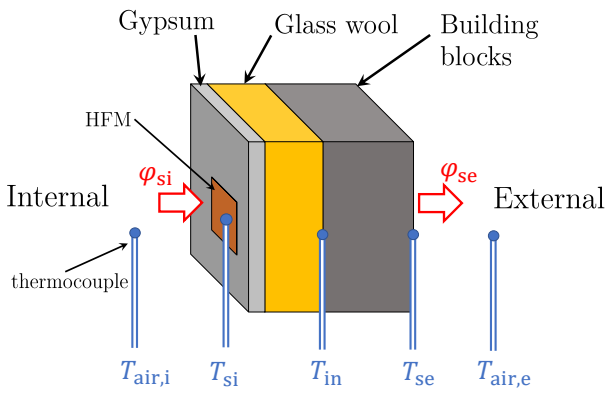

Figure 5: Location of main contact sensors.

3.3.1 Basics of IR thermography

The radiant intensity I received by the infrared camera is given by the so-called thermography equation:

$$I = \underbrace{\tau\varepsilon I^{\circ}\left(T_{\mathrm{s}}\right)}_{\text{emission}} + \underbrace{\tau\left(1-\varepsilon\right)I^{\circ}\left(T_{\mathrm{env}}\right)}_{\text{reflection}} + \underbrace{\left(1-\tau\right)I^{\circ}\left(T_{\mathrm{air}}\right)}_{\text{atmosphere emission}} \quad (7)$$

with ε the surface emissivity, τ the atmosphere transmittance, T_{s}, T_{env} and T_{air} respectively the surface, environment and air mean temperatures, and I° the black body radiant intensity (given by the Planck's law). The objects are supposed gray in the spectral bandwidth of the infrared camera. Thanks to its calibration curve, the camera converts the measured radiant intensities into apparent temperatures $T_{\mathrm{s}}^{\mathrm{app}}$. The apparent temperature of the surface is by definition the temperature of a black body that would emit a radiant intensity equal to the one received by the camera. The measurement of the absolute true temperature T_{s} from the apparent temperature $T_{\mathrm{s}}^{\mathrm{app}}$ requires knowledge of ε and T_{env} (also referred as the mean radiant temperature, MRT). The MRT may be measured with an infrared mirror (with a crumpled sheet of aluminum for instance). In the present application, the distance between the wall and the infrared camera is small (3 m) so that the influence of the atmosphere can be neglected: $\tau \approx 1$. The radiant intensity measured by the camera is considered to be proportional to T^4 according to the Stefan-Boltzmann law [60]. It comes:

$$T_{\mathrm{s}} = \left(\frac{T_{\mathrm{s}}^{\mathrm{app},4} - \left(1-\varepsilon\right)T_{\mathrm{env}}^{4}}{\varepsilon}\right)^{\frac{1}{4}} \quad (8)$$

Because of this dependence on ε and T_{env}, absolute temperature measurements with infrared thermography may be significantly biased [60]. However, IRT is much more accurate for measurements of temperature differences between objects of the same thermal image. When the temperature difference between two objects 1 and 2 is small (which is the case in building applications), it can be shown that:

$$T_{\mathrm{s1}} - T_{\mathrm{s2}} \approx \frac{T_{\mathrm{s1}}^{\mathrm{app}} - T_{\mathrm{s2}}^{\mathrm{app}}}{\varepsilon} \quad (9)$$

Thus, the temperature difference is directly proportional to the apparent temperature difference, and the multiplicative factor is the surface emissivity. In addition, the mean radiant temperature is no longer required which reduces measurement uncertainties.

The radiative heat flux is given by:

$$\varphi^{r} = \varepsilon\sigma_{\mathrm{SB}}\left(T_{\mathrm{s}}^{4} - T_{\mathrm{env}}^{4}\right) \quad (10)$$

with σ_{SB} the Stefan-Boltzmann constant. Temperature differences are small so that the radiative heat flux may be linearized:

$$\varphi^{r} \approx h^{r}\left(T_{\mathrm{s}} - T_{\mathrm{env}}\right) \quad (11)$$

with h^{r} the radiative heat transfer coefficient:

$$h^{r} = 4\varepsilon\sigma_{\mathrm{SB}}T_{\mathrm{m}}^{3} \quad (12)$$

with T_{m} a mean temperature. In first approximation, it may be taken equal to T_{s}, T_{env} or the average $\left(T_{\mathrm{s}} + T_{\mathrm{env}}\right)/2$. This choice is of little importance here given the small temperature differences at stake.

3.3.2 Implementation

The infrared camera monitors the wall internal surface temperature. Given the room dimensions, the distance between the setup and the sensor is too short for the wall to fit entirely within the camera field of view. Two solutions are implemented to fix this issue.

First, the wall is not built at the center of the chamber (between the two modules). As illustrated in Fig 6, it is rather built below one of the module, leaving about 3 m on the internal side. A cantilever structure above the wall allows splitting the room in two independent volumes, each one containing a regulation module. It is supported by one pole on each side as well as one in the middle.

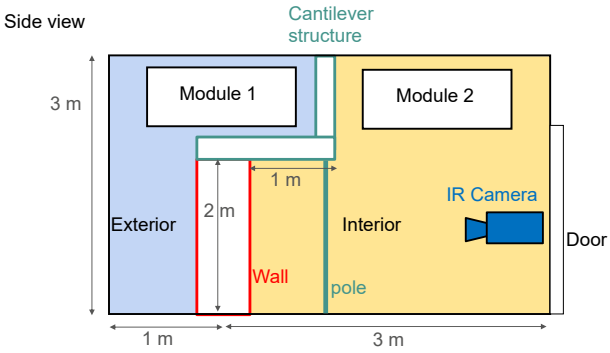

Figure 6: Scheme of the climate chamber layout.

Second, the camera is mounted on a rotating plateau. By spinning it back and forth between every image, it is possible to record two separate (thermographic) sequences of the scene: even frames focus on the left-hand side of the wall whereas odd frames focus on the right-hand side. The camera alternates between positions $-15°$ and $+15°$ ($0°$ corresponds to the normal to the wall). The images were corrected to compensate for this angle and also for the fish-eye distortion due to the wide-angle lens of the camera. Figure 7 displays an example of a thermogram captured in steady-state.

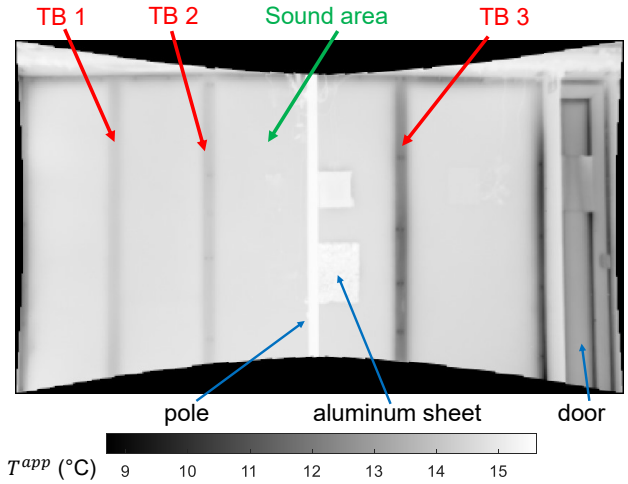

Figure 7: Reconstructed thermogram of the wall in steady-state.

A crumpled sheet of aluminum is fixed on the sound area of the wall. This is an infrared mirror: it enables to measure the mean radiant temperature T_{env}. The emissivity of this mirror was measured to 0.09. A thermocouple fixed on it allows compensating for this non-null emissivity.

3.4 Experimental tests

3.4.1 Steady-state: reference values

The wall is first characterized in steady-state and the values obtained are taken as references for validation of the novel active method. The two modules of the climate chamber are used to keep the internal and external air temperatures equal to 15 and -5°C respectively. This 20 K temperature difference is set for three days before performing the measurements, to ensure that a steady-state is reached (measured temperatures and heat fluxes do not vary more than 1%).

3.4.2 Active-tests: novel approach

For the active measurements, it was chosen to heat up the indoor air thanks to two 500 W electrical fan heaters (the internal chamber module is simultaneously switched off). This type of thermal load is easy to implement *in situ* and generates a rather uniform heating of the walls (unlike a radiant heat source for instance). Active tests last 7 to 8 h. Prior to this heating, the indoor air temperature $T_{\text{air,i}}$ is kept constant to 15°C for at least one day. Meanwhile, the external air temperature $T_{\text{air,e}}$ keeps being controlled by the chamber regulating system. Its setpoint temperature may be either constant or variable.

The example of an active test is presented in Fig 8 where the internal and external air temperatures are plotted. During the test, $T_{\text{air,i}}$ rises from 15°C to 32°C. On this example, $T_{\text{air,e}}$ is kept constant at 15°C (small oscillations are due to the chamber regulation system). However, in order to assess the robustness of the active characterization method to weather conditions, several configurations were tested with a varying external temperature. They are summarized in Tab 1. For each configuration, between 3 and 8 tests were undertaken to assess the method repeatability.

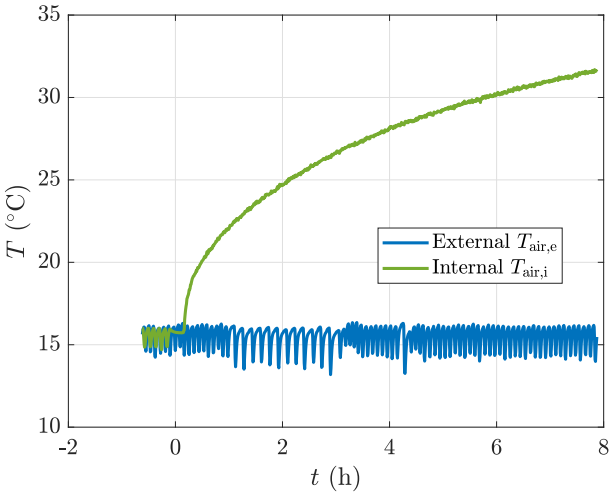

Figure 8: Internal and external air temperatures measured during an active test.

Table 1: Summary of active test configurations.

Config	$T_{\text{air,i}}$ (°C) (init. value)	$T_{\text{air,e}}$ (°C)	number of tests
1	15	5	5
2	15	15	3
3	15	$5 + 2.5\cos(\omega t)$	4
4	15	$5 + 5.0\cos(\omega t)$	4
5	15	$5 + 7.5\cos(\omega t)$	8
6	15	$15 + 7.5\cos(\omega t)$	3

In configurations 1 and 2, the external air temperature is kept constant. Measurements shown in Fig 8 were recorded during a test in configuration 2. In other configurations, $T_{\text{air,e}}$ is sinusoidal to mimic a day/night cycle. The peak-to-peak amplitude of the oscillations are varied from 5 to 15 K and the mean temperature is set to either 5°C or 15°C.

The oscillation period was set to 32 h instead of 24 h. This setting has a practical motivation: it enables to perform an active test every day at the same hour with a different $T_{\text{air,e}}$. This is illustrated in Fig 9 where temperatures are plotted for several consecutive days. The "inside wall" temperature plotted is measured on the interface between the glass wool and the concrete blocks. This simulates *in situ* experiments undertaken at different moments of the day. Given that low frequency thermal waves penetrate deeper a wall than high frequency ones, the chosen period of 32 h is a conservative choice.

4 Analysis method for steady-state measurements

Steady-state methods were used to determine references values for the wall thermal resistance R (sound area) and the

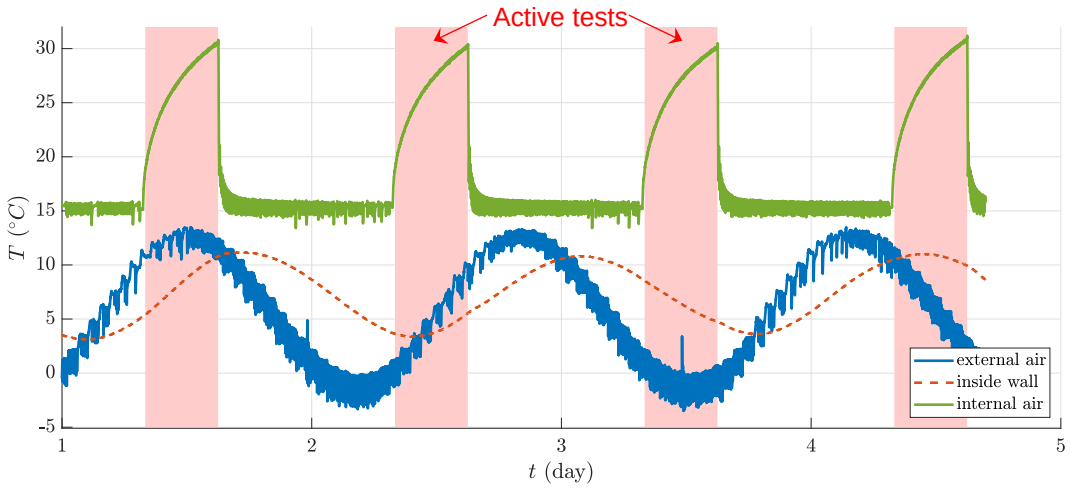

Figure 9: Example of internal and external temperatures for consecutive active tests (configuration 5).

transmission coefficients ψ of the thermal bridges. These references are useful to validate the active methodologies presented in Section 5.

4.1 Methodology

4.1.1 Sound area characterization

The thermal resistance of the wall without thermal bridge is measured according to ISO 9869-1 [61] averaged method from contact measurements performed on the sound area. One must check that the heat transfers are indeed 1D on this area. In practice, the uniformity of the surface temperature is assessed with an infrared camera. The internal and external surface temperatures, T_{si} and T_{se} respectively, are measured. The heat flux φ through the wall is measured with a HFM placed on the internal surface. Measured quantities are averaged over two hours to improve the signal to noise ratio by filtering out the small temperature oscillation induced by the climate chamber regulation system. The wall thermal resistance is given by:

$$R_{\text{wall}} = \frac{T_{\text{si}} - T_{\text{se}}}{\varphi} = \frac{\Delta T}{\varphi} \tag{13}$$

We also define the wall thermal transmittance:

$$U = \frac{1}{R_{\text{si}} + R_{\text{wall}} + R_{\text{se}}} \tag{14}$$

with $R_{\text{si}} = 0.13$ and $R_{\text{se}} = 0.04$ m^2.K.W^{-1} the internal and external superficial resistances. These are standards values used in the building sector [11] [62].

The uncertainties on R are propagated from measurement uncertainties on ΔT and φ [63]:

$$\text{u}(R) = R \times \sqrt{\left(\frac{\text{u}(\Delta T)}{\Delta T}\right)^2 + \left(\frac{\text{u}(\varphi)}{\varphi}\right)^2} \tag{15}$$

4.1.2 Thermal bridge characterization

The method is briefly recalled here and further details can be found in [58]. It is based on the incidence factor (or impact factor) I_{tb} initially introduced by Asdrubali *et al.* [52]. It is the ratio of the global thermal transmittance U_{tb} of the wall with thermal bridge over the transmittance U_{1D} of the same wall without thermal bridge (sound area). In steady-state, I_{tb} can also be expressed as a heat flux ratio:

$$I_{\text{tb}} = \frac{U_{\text{tb}}}{U_{\text{1D}}} \overset{\text{steady-state}}{=} \frac{\overline{\varphi_{\text{tb}}}}{\varphi_{\text{1D}}} \tag{16}$$

with the upper bar $\overline{-}$ denoting the mean value (space average). By definition, heat transfers are not one-dimensional on thermal bridges.The expression of the linear thermal bridge transmittance ψ given in Eq 3 may be re-written as:

$$\psi = L_{\text{tb}} U_{\text{1D}} (I_{\text{tb}} - 1) \tag{17}$$

The heat flux ratio is supposed equal to the radiative heat flux ratio:

$$I_{\text{tb}} = \frac{\overline{\varphi^r_{\text{tb}}}}{\varphi^r_{\text{1D}}} \tag{18}$$

This assumption is justified if several conditions are met. First, the air and mean radiant temperatures have to be close. This is a realistic hypothesis indoor, in steady-state, inside a well insulated room. Second, the surface emissivity as well as the convective and radiative heat transfer coefficients (h^c and h^r respectively) have to be uniform on the thermal bridge and the sound area. This is also realistic given the small temperature contrasts at stake. By expressing radiative heat fluxes as a function of apparent temperatures, Eq 18 becomes:

$$I_{\text{tb}} = \frac{\overline{T^{\text{app}}_{\text{tb}}} - T^{\text{app}}_{\text{env}}}{T^{\text{app}}_{\text{1D}} - T^{\text{app}}_{\text{env}}} \tag{19}$$

In theory, T_{1D} is uniform around the thermal bridge. In practice however, the temperature on each side of the thermal bridge may be slightly different. If so, T_{1D} becomes the average of the surface temperatures measured on each side of the thermal bridge.

This approach is interesting because only apparent temperatures are needed to work out the incidence factor I_{tb}. Thus, the values of the wall emissivity and the heat transfer coefficients are not needed. The ψ-value is then calculated using Eq 17. The uncertainty over the estimated transmittance is propagated from uncertainties over L_{tb}, U_{1D} and I_{tb}.

It is smaller than that of the original method from [52] (see [58] for more details).

4.2 Results

4.2.1 Wall thermal resistance

The results obtained from measurements on the sound area are summarized in Tab 2. The heat flux through the wall and the internal/external temperature differences are about 5 $W.m^{-2}$ and 19 °C, respectively. The overall wall thermal resistance is estimated to $R_{wall} = 3.49 \pm 0.11$ $m^2.K.W^{-1}$. This corresponds to an air-to-air overall thermal transmittance $U_{1D} = 0.27 \pm 0.01$ $W.m^{-2}.K^{-1}$. In addition, the thermal resistance of the insulation system (gypsum + glass wool) is estimated to $R_{insul} = 3.15 \pm 0.10$ $m^2.K.W^{-1}$. This latter value could be obtained from a thermocouple measurement inside the wall.

Table 2: Measured quantities and calculated thermal resistance (ISO 9869-1 [61]).

	Whole wall	Insulation system (gypsum+glass wool)
ΔT_{sie} (K)	18.9 ± 0.1	16.9 ± 0.1
φ_{si} $(W.m^{-2})$	$5.35 \pm 3\%$	$5.35 \pm 3\%$
R $(m^2.K.W^{-1})$	3.49 ± 0.11	3.15 ± 0.10
U $(W.m^{-2}.K^{-1})$	0.27 ± 0.01	-

4.2.2 Measurements on thermal bridges

Figure 10 presents thermograms captured on each thermal bridge (they are extracted from Fig 7). They are the result of an average of thermograms captured during two hours of steady-state. In addition, Fig 11 plots the apparent temperature profiles obtained from vertical average of these thermograms. The apparent temperature of the mirror (crumpled aluminum sheet) is also plotted.

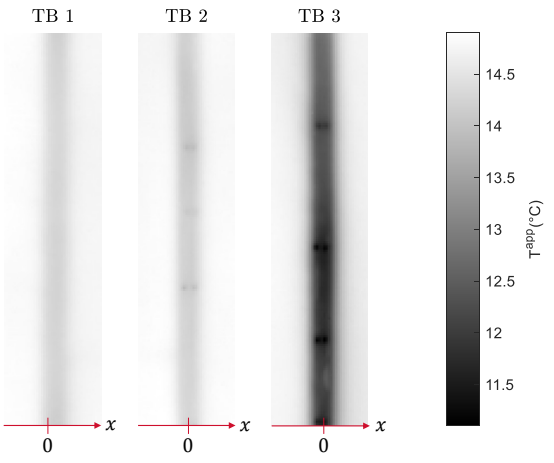

Figure 10: Thermograms of thermal bridges in steady-state.

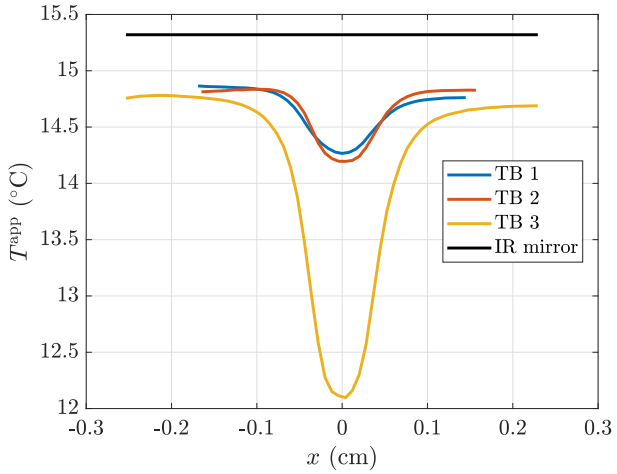

Figure 11: Measured apparent temperature profiles T_{tb}^{app} on thermal bridges in steady-state as well as mean radiant temperature T_{env}^{app}.

As expected, the temperature contrast is much higher on TB 3 than on the other thermal bridges. In addition, the temperature is almost invariant with the altitude: the regulation modules of the climate chamber prevents air stratification. The small black dots on TB 2 and TB 3 are the screws holding the gypsum board to the metal frame. It may also be noticed that the measurement noise is very small. Indeed, not only has the cooled sensor of the camera a small sensitivity (20 mK), the profiles are also obtained from space and time averages of many thermograms.

4.2.3 ψ-value calculations

The apparent temperature profiles shown in Fig 11 are used to work out the thermal bridge incidence factor I_{tb} (Eq 19) which is required in the estimation of the ψ coefficient (Eq 17).

The thermal bridge width L_{tb} also has to be set. An interesting result is that the measured ψ-values are rather robust to the choice of L_{tb}. As this length increases, the incidence factor I_{tb} decreases as shown in Fig 12. This result is physical because when L_{tb} is large, φ_{tb} in Eq 16 is obtained from average over a larger zone mainly containing the sound area. However, ψ rapidly reaches a plateau as L_{tb} increases (see Fig 13): the increase in L_{tb} compensates for a decrease in I_{tb}. This property is also predicted by the theory. However, the uncertainty on ψ keeps increasing with L_{tb} because the magnitude of I_{tb} tends to zero. For the wall considered, the temperature profile to select for the analysis needs to have a width L_{tb} approximately above 20 cm for TB 1 and TB 2 and above 30 cm for TB 3. Thus, $L_{tb} = 30$ cm is set for each thermal bridge.

In addition, the ψ-value is rather independent on the altitude of the measurement, as shown in figures 14, 15 and 16. The screws are clearly visible on ψ profiles for TB 2 and TB 3.

Finally, the measured thermal bridges transmission coefficients and their uncertainty are summarized in Tab 3. These values are obtained from average over the whole height of the thermal bridges. Additional heat losses due to TB 3 are about four times superior than those due to TB 1 and TB 2.

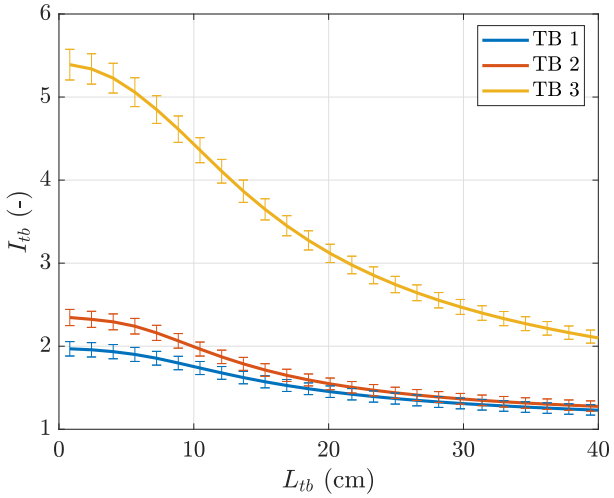

Figure 12: Impact of L_{tb} on measured I_{tb} for each thermal bridge.

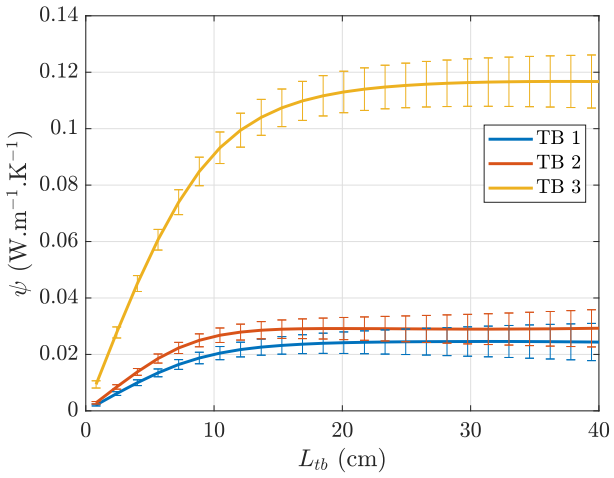

Figure 13: Impact of L_{tb} on measured ψ for each thermal bridge.

In addition, TB 2 has a slightly higher ψ-value than TB 1. This small difference is explained by the presence of a joint between two gypsum boards and the screws on TB 2.

5 Presentation of new analysis method (active method)

5.1 General method

The active method presented here aims at characterizing a thermal bridge heat losses *in situ*. It is summarized in Fig 17. The method is described from bottom to top:

- The estimation of the thermal bridge transmission coefficient ψ or χ requires the values of two thermal resistances (see equations 3 and 14). The first one is the resistance $R_{1\text{D}}$ of the nearby sound area. The second one is the equivalent resistance R_{tb} of the section of the wall impacted with the thermal bridge.

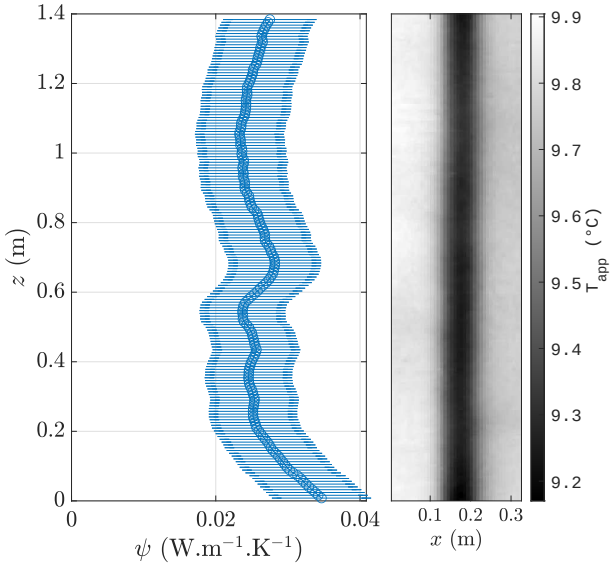

Figure 14: Impact of altitude z on measured ψ coefficient and thermal image for TB 1.

Table 3: Thermal bridge transmission coefficients estimated in steady-state.

Thermal bridge	I_{tb} (-)	ψ (mW.m^{-1}.K^{-1})
TB 1	1.31 ± 0.06	26 ± 5
TB 2	1.34 ± 0.07	30 ± 5
TB 3	1.90 ± 0.07	117 ± 8

- Estimation of $R_{1\text{D}}$:
  - Thermal resistance $R_{1\text{D}}$ is estimated with the active method introduced by the authors in [13] and presented in section 5.2. This technique, developed for the characterization of a homogeneous wall, is based on an inverse technique using a white-box model. It relies on simultaneous measurement of the wall internal surface temperature T_{si} and heat flux φ_{si}. The measurement of the external wall surface temperature T_{se} may also be required.
  - The internal surface temperature and heat flux on the sound area, noted $T_{\text{si}}^{1\text{D}}$ and $\varphi_{\text{si}}^{1\text{D}}$, are measured with contact sensors (thermocouples and heat flux meters).
- Estimation of R_{tb}:
  - The equivalent thermal resistance R_{tb} of the section of the wall affected by the thermal bridge is estimated with the same active method: this wall area is treated as a homogeneous wall of equivalent thermal properties. Indeed, several authors proved that a non-homogeneous wall could be modeled with an equivalent multi-layer homogeneous wall having the same thermal behavior (see Martin *et al.* [32] and Quinten *et al.* [35] for instance). The mean thermal bridge internal surface temperature $\overline{T_{\text{si}}^{\text{tb}}}$ and heat flux $\overline{\varphi_{\text{si}}^{\text{tb}}}$ are fed

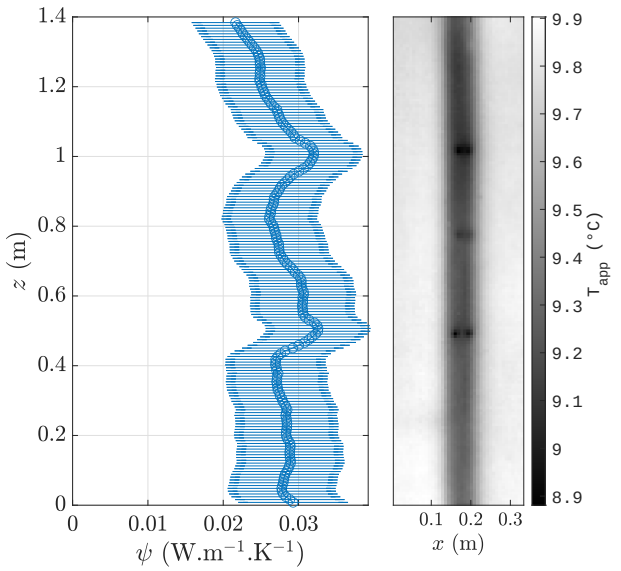

Figure 15: Impact of altitude z on measured ψ coefficient and thermal image for TB 2.

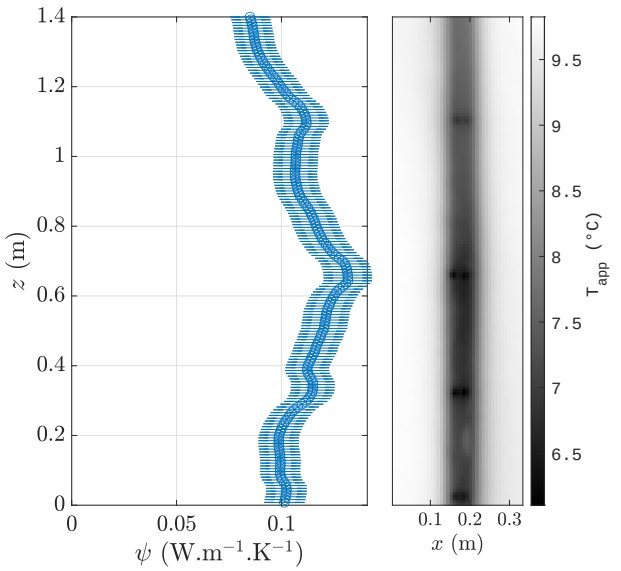

Figure 16: Impact of altitude z on measured ψ coefficient and thermal image for TB 3.

to the inverse method. These quantities are averaged over the thermal bridge area of influence defined by L_{tb} for a linear thermal bridge and A_{tb} for a point thermal bridge.

– The fields of surface temperature $T_{\text{si}}^{\text{tb}}$ and heat flux $\varphi_{\text{si}}^{\text{tb}}$ on the thermal bridge must be measured. Contact sensors are not applicable here since heat transfers are not 1D. In addition, using many sensors to capture the surface temperature and heat flux fields would be very intrusive and time consuming. Instead, $T_{\text{si}}^{\text{tb}}$ and $\varphi_{\text{si}}^{\text{tb}}$ are extrapolated from their counterparts $T_{\text{si}}^{\text{1D}}$ and $\varphi_{\text{si}}^{\text{1D}}$ measured with contact sensors on a nearby sound area. The extrapolation is performed thanks to infrared thermography measurements as well as quantification of the total heat transfer coefficient h. This extrapolation process was developed and validated by the authors in [14]. It is presented in section 5.3.1.

– The temperature difference $T_{\text{si}}^{\text{tb}} - T_{\text{si}}^{\text{1D}}$ is measured with infrared thermography. The wall emissivity ε is required. to work out true temperature difference form the apparent temperature difference (see Eq 9).

– The overall heat transfer coefficient h on the wall surface is measured is a specific device based on a harmonic excitation (see section 5.3.2).

One of the main advantage of this methodology is that it is not intrusive. Indeed, apart from a HFM fixed near the thermal bridge (and for some cases a thermocouple on the other side of the wall), no contact sensor is used. The inverse method as well as the temperature and heat flux extrapolation process are detailed below.

5.2 Inverse method for homogeneous wall characterization

The inverse method is briefly presented in this section. For more information, please refer to [13]. The method is based on four main steps:

1. Perform active measurements
2. Define an analytical expression of the model input
3. Generate direct model
4. Estimate parameters: minimize difference between model and measurements

These four stages are detailed below. An active test of configuration 2 (the one already introduced in Fig 8) is taken as an example to illustrate the method. Temperatures and heat fluxes are measured on the sound area.

5.2.1 Perform active measurements

As presented in section 3.4, the indoor air is heated for several hours. The surface temperature T_{si} and heat flux φ_{si} measured during the chosen example are plotted in Fig 18. Initial conditions were subtracted so that only variations in temperature and heat flux are accounted for. The heat flux is considered positive when it flows from the environment to the wall surface.

5.2.2 Define an analytical expression of the model input

Temperatures are taken as input of the direct model. The thermal quadrupole formalism (see next section) requires to have an analytical expression of the Laplace transform of these temperatures. This expression is obtained from a fit of a function of known Laplace transform on the measurements. This function does not need to have any physical meaning. The following function (polynomial in 1/j) proved to work well on T_{si}:

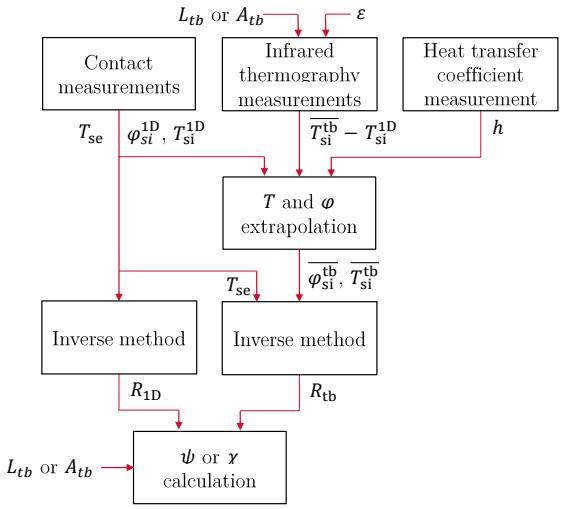

Figure 17: Flow chart of the active method for thermal bridge characterization.

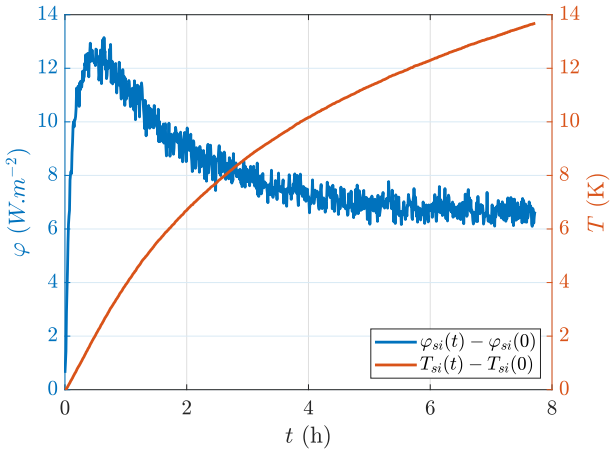

Figure 18: Measured surface temperature and heat flux variations during an active test (configuration 2).

$$T(\boldsymbol{\alpha}, t) = \sum_{j=1}^{n} \alpha_j t^{1/j} \tag{20}$$

where coefficients α_k are estimated by a least-square fit. The Laplace transform of this function is:

$$\widetilde{T}(\boldsymbol{\alpha}, p) = \sum_{j=1}^{n} \alpha_j \frac{\Gamma\left(\frac{1}{j}+1\right)}{p^{\frac{1}{j}+1}} \tag{21}$$

with Γ the Gamma function. The order n is increased until the difference between the measurements and the fitted function stops decreasing. The choice $n = 7$ proved to work well [13].

5.2.3 Direct model formulation

The thermal quadrupole formalism [64] is very convenient to model one-dimensional multi-layer heat conduction problems. In the Laplace domain, relations between surface temperatures and heat fluxes are simply given by 2-by-2 matrix multiplications:

$$\begin{bmatrix} \widetilde{T_{si}} \\ \widetilde{\varphi_{si}} \end{bmatrix} = \prod_{k=1}^{n_L} \begin{bmatrix} A_k & B_k \\ C_k & D_k \end{bmatrix} \times \begin{bmatrix} \widetilde{T_{se}} \\ \widetilde{\varphi_{se}} \end{bmatrix} \tag{22}$$

with n_L the number of layers, superscript $\sim$ denoting Laplace transforms and:

$$A_k = D_k = \cosh\left(R_k b_k \sqrt{p}\right) \tag{23}$$

$$B_k = \sinh\left(R_k b_k \sqrt{p}\right) / \left(b_k \sqrt{p}\right) \tag{24}$$

$$C_k = \sinh\left(R_k b_k \sqrt{p}\right) \times b_k \sqrt{p} \tag{25}$$

with R_k and b_k the thermal resistance and thermal effusivity of the k^{th} layer and p the Laplace variable. We introduce the following notation:

$$\begin{bmatrix} A_{1-n} & B_{1-n} \\ C_{1-n} & D_{1-n} \end{bmatrix} = \prod_{k=1}^{n} \begin{bmatrix} A_k & B_k \\ C_k & D_k \end{bmatrix} \tag{26}$$

for $1 \leq n \leq n_L$. The De Hoog algorithm [65] is used to numerically calculate the inverse Laplace transforms and generate data in the time domain.

5.2.4 Choice of direct model

Two models are used, depending on the configuration (weather conditions). They will be referred as model A and model C to match notations used in [13]. The models are presented in Fig 19. Model C may rely on results obtained from model D. Temperature T_{in} and heat flux φ_{in} are not used for the estimation: there is no need to implement contact sensors inside the wall. These quantities are only presented here for a better understanding of the problem. The same models are applied to the sound area and the thermal bridges.

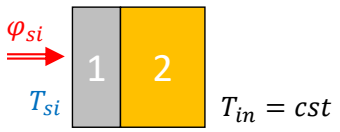

(a) Model A.

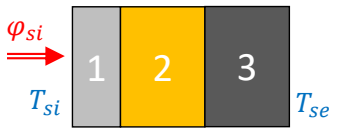

(b) Model C.

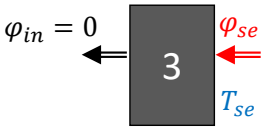

(c) Model D.

Figure 19: Scheme of the 1D models.

If the external temperature is constant (configurations 1 and 2), only indoor measurements are required. The temperature T_{in} between the glass wool and the building blocks is

assumed constant, therefore only the first two layers (gypsum and glass wool for the sound area, equivalent layers for the thermal bridges) are modeled. The properties of the third layer (building blocks) are not estimated but this is not a problem since we are interested here in this difference induced by the presence of thermal bridges. The third layer does not contribute to the difference in thermal resistance because it is the same on thermal bridges and on the sound area. This model (model A), is given by:

$$\widetilde{\varphi_{\mathrm{si}}} = \frac{D_{1-2}(\boldsymbol{\beta})}{B_{1-2}(\boldsymbol{\beta})}\widetilde{T_{\mathrm{si}}} \tag{27}$$

with $\boldsymbol{\beta} = [R_1,\ b_1,\ R_2,\ b_2]^{\mathrm{T}}$ the unknown parameter vector.

If the external temperature varies (configurations 3 to 6), the external surface temperature T_{se} must be measured as well and the third layer must be included in the model (model C):

$$\widetilde{\varphi_{\mathrm{si}}} = \frac{D_{1-3}(\boldsymbol{\beta})}{B_{1-3}(\boldsymbol{\beta})}\widetilde{T_{\mathrm{si}}} + \frac{1}{B_{1-3}(\boldsymbol{\beta})}\widetilde{T_{\mathrm{se}}} \tag{28}$$

with $\boldsymbol{\beta} = [R_1,\ b_1,\ R_2,\ b_2,\ R_3,\ b_3]^{\mathrm{T}}$. However, as detailed in [13], this problem is too ill-posed: the six parameters in $\boldsymbol{\beta}$ cannot be estimated simultaneously from a single experiment. Thus, R_3 and b_3 have to be supposed known in the inverse problem. Reference values may be used, if available. If not, R_3 and b_3 may be estimated separately from measurements of the external surface heat flux φ_{se} and another model (model D) taking $\varphi_{\mathrm{in}} = 0$ as boundary condition:

$$\widetilde{\varphi_{\mathrm{se}}} = \frac{C_3(\boldsymbol{\beta})}{B_3(\boldsymbol{\beta})}\widetilde{T_{\mathrm{se}}} \tag{29}$$

with $\boldsymbol{\beta} = [R_3,\ b_3]^{\mathrm{T}}$.

5.2.5 Parameter estimation

The estimation of the unknown parameters is performed by minimizing the cost function J which is the quadratic difference between the model prediction $\boldsymbol{\varphi}_{\mathrm{mo}}$ and the measurements $\boldsymbol{\varphi}$:

$$J(\boldsymbol{\beta}) = \sum_{i=1}^{m} \left(\varphi(t_i) - \varphi_{\mathrm{mo}}(\boldsymbol{\beta}, t_i)\right)^2 \tag{30}$$

with m the number of measurement points. Because the model is not linear, the minimization process is iterative. The Levenberg-Marquardt algorithm (described in [66], [67] and [68]) was used to perform this minimization. It was chosen for its robustness.

The model is supposed unbiased and measurements are supposed corrupted with a white noise $\boldsymbol{\varepsilon}$ of standard deviation σ:

$$\boldsymbol{\varphi} = \boldsymbol{\varphi}_{\mathrm{mo}}(\boldsymbol{\beta}) + \boldsymbol{\varepsilon} \tag{31}$$

We define the reduced sensitivity coefficients [69]:

$$\boldsymbol{X}^*(\beta_j) = \beta_j \frac{\partial \boldsymbol{\varphi}_{\mathrm{mo}}}{\partial \beta_j} \tag{32}$$

and the variance-covariance matrix:

$$\mathrm{cov}\left(\widehat{\boldsymbol{\beta}}\right) = \sigma^2 \left(X^{*\mathrm{T}} X^*\right)^{-1} \tag{33}$$

$$\mathrm{cov}\left(\widehat{\boldsymbol{\beta}}\right) \approx \begin{bmatrix} \mathrm{var}\left(\widehat{\beta}_i\right) & \mathrm{cov}\left(\widehat{\beta}_i, \widehat{\beta}_j\right) & \cdots \\ & \mathrm{var}\left(\widehat{\beta}_j\right) & \cdots \\ \mathrm{sym} & & \ddots \end{bmatrix} \tag{34}$$

as well as the hybrid matrix V_{cor}:

$$\mathrm{V_{cor}}\left(\widehat{\boldsymbol{\beta}}\right) \approx \begin{bmatrix} \sqrt{\mathrm{var}\left(\widehat{\beta}_i\right)}/\widehat{\beta}_i & \rho_{ij} & \cdots \\ & \sqrt{\mathrm{var}\left(\widehat{\beta}_j\right)}/\widehat{\beta}_j & \cdots \\ \mathrm{sym} & & \ddots \end{bmatrix} \tag{35}$$

where ρ_{ij} are correlation coefficients:

$$\rho_{ij} = \frac{\mathrm{cov}\left(\widehat{\beta}_i, \widehat{\beta}_j\right)}{\sqrt{\mathrm{var}\left(\widehat{\beta}_i\right)\mathrm{var}\left(\widehat{\beta}_j\right)}} \tag{36}$$

These matrices are symmetrical. They are defined locally around a nominal value of the parameters, and so are the reduced sensitivity coefficients. This is due to the non-linear structure of the direct model.

The analysis of the reduced sensitivity coefficients as well as the V_{cor} matrix are useful to determined the well-posedness of the inverse problem. In other words, it may help to define the best experiment to carry out and then enable to detect which parameters may or may not be estimated from the given experiment.

The example chosen for this section belongs to configuration 2: the external temperature is constant. Thus, model A (Eq 27) is used. The corresponding reduced sensitivity coefficients are plotted in Fig 20. Reference values for the sound area were allocated to the parameters. They have different origins. The thermal conductivity and diffusivity of the gypsum were measurements in laboratory with the Hot Disk method [70]. From these quantities as well as the board thickness, the thermal resistance and effusivity are calculated ($R_1 = 0.05$ m^2.K.W^{-1} and $b_1 = 421$ J.K^{-1}.m^{-2}.s$^{-1/2}$). The glass wool properties are manufacturer data ($R_2 = 3.12$ m^2.K.W^{-1}) and standard value from the literature [71] ($b_2 = 21$ J.K^{-1}.m^{-2}.s$^{-1/2}$, calculated from thermal conductivity and diffusivity).

The V_{cor} matrix (calculated with $\sigma = 0.4$ W.m^{-2}, representative of an experiment) is:

$$V_{\mathrm{cor}} = \begin{bmatrix} 0.15 & -0.98 & -0.29 & -0.61 \\ & 0.07 & 0.25 & 0.49 \\ & & 0.02 & 0.52 \\ \mathrm{sym} & & & 0.09 \end{bmatrix} \tag{37}$$

The parameter of interest is R_2 (thermal resistance of the insulation layer, where thermal bridges are located). It has a non negligible reduced sensitivity and is not correlated to any other parameter: its relative estimation uncertainty is of 2%. Parameters R_1 and b_1 have a higher reduced sensitivity but are correlated (sensitivity curves of similar shape and high correlation coefficient) so their relative uncertainty is higher than that of R_2: 15 and 7% respectively. Finally, b_2 has a

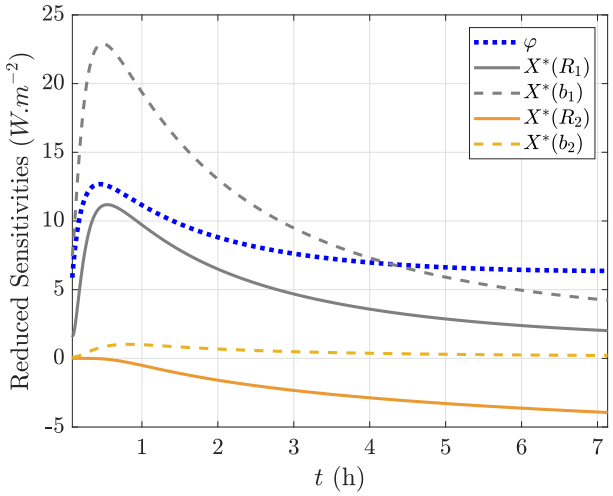

Figure 20: Evolution of reduced sensitivity coefficients for the configuration 2 of active tests.

very small reduced sensitivity so its relative uncertainty is also higher: 9%. For a more detailed sensitivity analysis, please refer to [13].

Consequently, the current problem is well-posed enough for an accurate estimation of R_2 to be possible.

5.3 Measurement of surface temperature and heat flux fields on thermal bridges

To generalize the previous inverse method to a non-homogeneous wall, such as a wall containing thermal bridges, one needs to know the surface temperature and heat flux fields over the wall. The chosen approach consists in measuring these quantities on a sound area with contact sensors and then extrapolating these measurements to thermal bridges. Provided that the emissivity of the wall is known, the extrapolation of the temperature is rather straightforward with IRT using Eq 9. Nevertheless, the extrapolation of the total heat flux is more complex and is detailed here.

5.3.1 Heat flux extrapolation

The heat flux φ_s on the surface of a wall at temperature T_s is given by the sum of the convective and radiative heat fluxes:

$$\varphi_s = h^c \left(T_s - T_{air}\right) + h^r \left(T_s - T_{env}\right) \tag{38}$$

where h^c and h^r are the convective and linearized radiative heat transfer coefficients respectively. Without loss of generality, the surface heat flux may also be expressed as:

$$\varphi_s = h \left(T_s - T_{op}\right) \tag{39}$$

with $h = h^c + h^r$ the total heat transfer coefficient and $T_{op} = \left(h^c T_{air} + h^r T_{env}\right)/h$ the so called "operative temperature". Therefore, the quantification of φ requires knowledge of T, T_{op} and h. The *in situ* measurement of the operative temperature is very complex. The following assumption is usually made: $T_{op} = T_{air}$. While this is reasonable indoor in steady-state conditions inside a well-insulated building, T_{air} and T_{env} might be significantly different in many cases. This assumption especially not valid in the current context of active measurements: when the heaters are turned on, the air is significantly hotter than the surrounding walls. The duration of the experiment is too short for the room to reach a new thermal equilibrium. In addition, even T_{air} is not well defined because it is not uniform inside the room,mainly because of air stratification. Indeed, unlike for steady-state measurements, the regulation system of the climate chamber is turned off and electric fan heaters are used instead. This more realistic configuration leads to some air stratification. To overcome this problem, it is preferable to express the heat flux φ_{tb} on thermal bridges as a function of the heat flux φ_{1D} measured with a HFM on a sound area. From Eq 39, and assuming that h and T_{op} are uniform on the two zones, it comes:

$$\varphi_{tb} = \varphi_{1D} + h \left(T_{tb} - T_{1D}\right) \tag{40}$$

The main advantage is that the operative temperature is no longer needed. The temperature difference $T_{tb} - T_{1D}$ is obtained from IRT (see Eq 9):

$$T_{tb} - T_{1D} = \frac{T_{tb}^{app} - T_{1D}^{app}}{\varepsilon} \tag{41}$$

The wall emissivity ε is also supposed uniform on the sound area and the thermal bridge. The total heat transfer coefficient h is measured with a specific device presented in the next section. The heat flux extrapolation procedure was validated in [14].

5.3.2 Overall heat transfer coefficient measurement

The main challenge consists in quantifying the local heat transfer coefficient without knowing the operative temperature. For this purpose, the authors developed and tested several *in situ* measurements methods of h overcoming this issue (see [14] and [72]).

The method selected here is the one referred as the "Harmonic Excitation" (HE) method in [14]. It was chosen for its robustness and ease of implementation. It is based on a sinusoidal thermal load. The sensor (or "h-meter") used is presented in Fig 21. It is made out of an array of nine thermoelectric coolers (TEC) sandwiched between two 20×20 cm^2 aluminum boards. The boards are 1 mm thick and are useful to homogenize temperature on each side of the TECs. A HFM, inside which a T-type thermocouple is embedded, is fixed on the front face of the device. Like other HFMs used in the experiments, it is covered with adhesive tape of same infrared emissivity as the wall. The device is rather thin (5 mm) and is supposed non-intrusive.

The voltage applied to the array of TECs is sinusoidal (with a frequency f) so that both the surface temperature and heat flux are sinusoidal as well. The measurement methods is presented in further details in appendix A. It enables to estimated the heat transfer coefficient. The estimation uncertainty is also calculated.

It was noticed that the heat transfer coefficient was rather constant during active tests. Therefore, the extrapolation is performed with a constant h value. This has the advantage of reducing noise on extrapolated quantities.

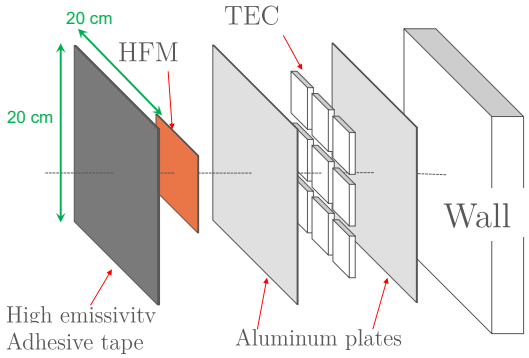

Figure 21: Scheme of the "h-meter" fixed on the wall.

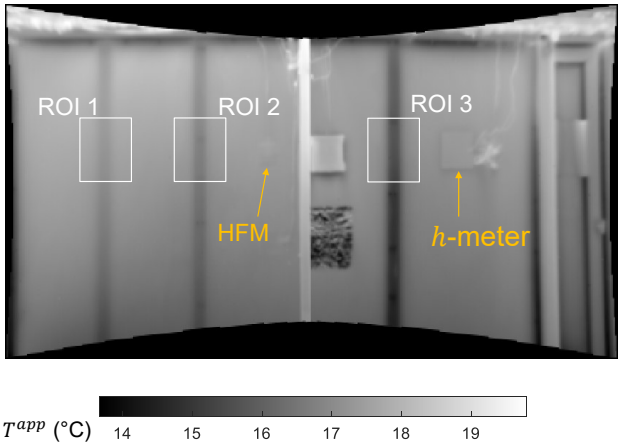

Figure 23: Thermal image captured during an active test (configuration 2, after 4 h of heating) and regions of interest (ROI) used for heat flux extrapolation.

6 Active (dynamic) results

6.1 Detailed results on one example

Results are detailed on the active test of configuration 2 already presented above.

6.1.1 Heat flux extrapolation

The measured temperature differences $\Delta T = T_{1D} - T_{tb}$ between the sound area and the three thermal bridges are plotted in Fig 22. These temperatures, obtained from infrared thermography, are space averages over the regions of interest (ROI) shown in Fig 23. The ROIs were placed at the same altitude as the h-meter and the HFM. Indeed, because of air stratification, the heat transfer coefficient may not be quite uniform all over the wall height whereas the extrapolation process is based on a uniformity assumption. As with steady-state calculations, L_{tb} (width of the ROIs) is set to 30 cm.

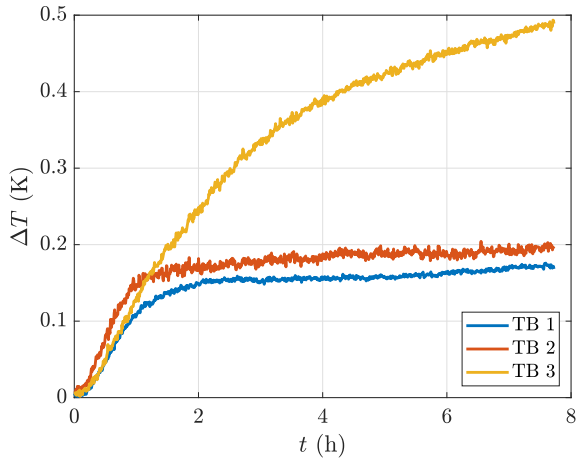

Figure 22: Evolution of temperature differences between thermal bridges and sound area (from IRT) during an active test (configuration 2).

At the beginning of the experiment, the temperature differences are null because the wall is at thermal equilibrium. Then, they are positive because the temperature on thermal bridges is lower than that on the sound area. The heat transfer coefficient is estimated to 9.6 ± 0.5 W.m^{-2}.K^{-1}. This is above the standard value of 7.7 W.m^{-2}.K^{-1} for indoor building walls [62]. The difference is due to the heating of the air which generate air movements and therefore increases convective heat losses. The measured h-value of 9.6 W.m^{-2}.K^{-1} is in good agreement with measurements undertaken in similar conditions in [14].

Surface temperatures and heat fluxes are then extrapolated from the sound area to thermal bridges. These quantities are plotted in Figures 24 and 25. Temperature contrasts are very small (about 0.2 K) when compared to the temporal evolution of temperatures (about 15 K): the curves are hardly distinguishable. Nevertheless, these small temperature contrasts lead to much more noticeable heat flux contrasts. The heat flux on TB 3 slightly increases at the end of the experiment whereas it keeps decreasing on the other zones. This result looks odd but it is physical, as proved in the parameter estimation below.

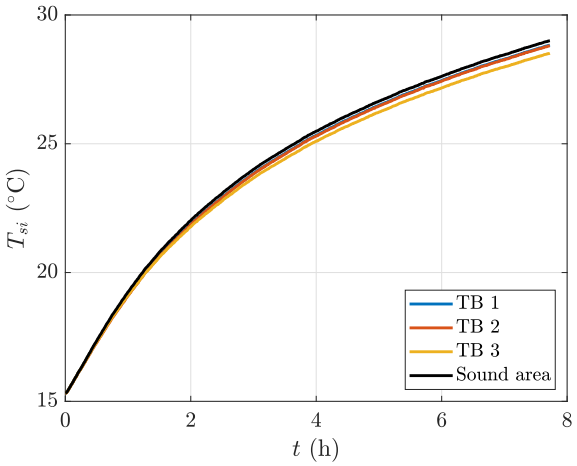

Figure 24: Evolution of temperature extrapolated from the sound area to the thermal bridges.

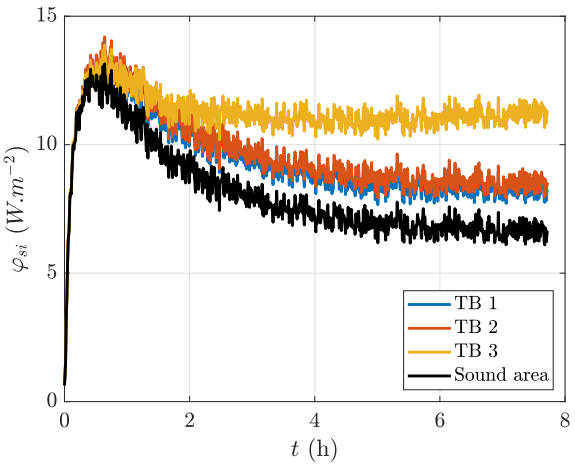

Figure 25: Evolution of heat flux extrapolated from the sound area to the thermal bridges.

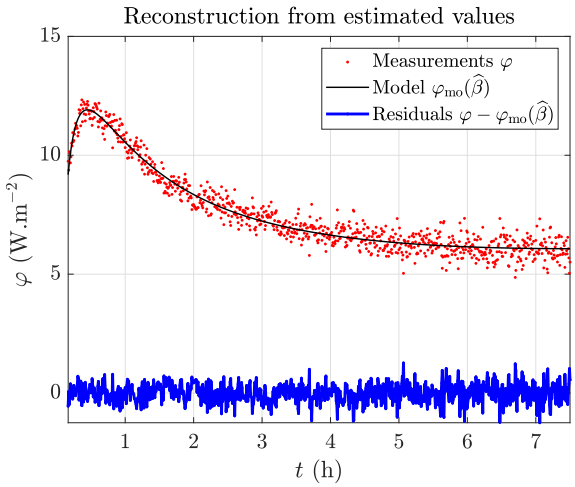

Figure 26: Comparison of measurements and model output after parameter estimation (sound area).

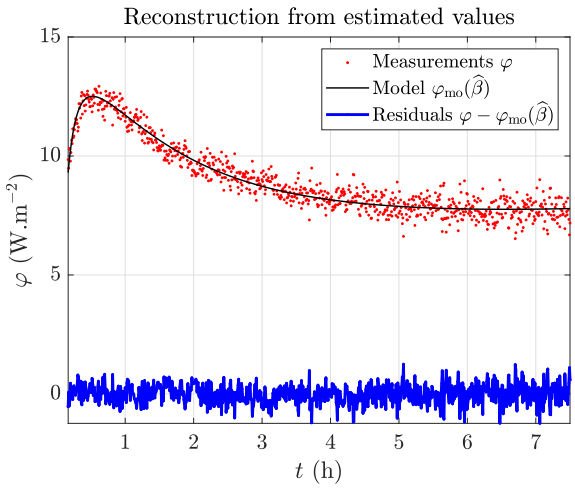

Figure 27: Comparison of measurements and model output after parameter estimation (TB 1).

It may be noticed that heat flux curves in Fig 25 have a highly correlated noise. This is because the noise on the heat flux increment $h\,(T_{\text{tb}} - T_{1\text{D}})$ is much smaller that the noise on $\varphi_{1\text{D}}$ measured with a HFM.

6.1.2 Parameter estimation

Figure 26 compares the measured surface heat flux φ_{si} on the sound area to the model prediction $\varphi_{\text{mo}}\left(\widehat{\boldsymbol{\beta}}\right)$ after estimation of parameters $\widehat{\boldsymbol{\beta}}$. Figures 27, 28 and 29 present the same quantities for TB 1, TB 2 and TB 3 respectively. The residuals (difference between model and measurements) are not signed: they have the shape of a white noise. The residuals standard deviation is equivalent to the noise level: 0.4 W.m^{-2}. This is a prerequisite for the parameter estimation to be correct. It proves that the model can reconstruct the measurements and the only remaining difference is the measurement noise. The first 10 minutes of the experiment were removed because HFM measurements are inaccurate at the beginning of the heating phase (the heat flux increases too fast). It was also shown that an active test of about 6 h is enough here for the parameter estimation to be accurate [13].

The estimated parameters and their associated uncertainties are gathered in Tab 4. The parameter reference values for the sound area presented in Section 5.2.5 are included in the table. The method successfully estimates the thermal properties of the insulation system (sound area). In particular, the main parameter of interest, R_2, is only about 5% away from its reference value. In addition, the estimated thermal resistance of the insulation system $\widehat{R_1} + \widehat{R_2}$, is equal to 3.09 m^2.K.W^{-1}. This value is in good agreement with results steady-state measurements from ISO 9869-1 [61]: 3.15 m^2.K.W^{-1} (see Tab 2).

As expected, the equivalent resistance R_2 of the thermal bridges are smaller than that of the sound area (especially for TB 3). The estimated thermal effusivity b_2 is also higher on thermal bridges because of the higher thermal inertia of metallic rails when compared to glass wool. The estimated properties of the gypsum layer (R_1 and b_1) are approximately the same on the sound area and the thermal bridges. For the calculation of thermal bridge transmittance coefficient ψ, only the value of the thermal resistances (especially R_2) are required.

On this example, the two-layer model A (Eq 27) was used because the external temperature is constant. In this model, temperature T_{in} between the insulation system and the building blocks is supposed to remain constant during the active test. This assumption is valid for the sound area, TB 1 and TB 2 (this was checked using thermocouples placed inside the wall). However, the metallic rail of TB 3 crosses the insulation layer entirely and is directly in contact with the third layer. Thus, T_{in} does no remain constant on TB 3. However, on the ROI used on thermal images for the extrapolation of surface temperature and heat flux (see ROI 3 in Fig23), the thermal bridge itself only represents a small area. Temperature differences shown in Fig 22 arise from average over the thermal bridge and its surrounding where T_{in} is less affected. As a consequence, the assumption T_{in} = constant in model A is deemed valid also for TB 3. Results presented below prove that this model is able to correctly estimate the transmittance

Table 4: Summary of parameter estimation on sound area and thermal bridges.

		Reference values	Estimated values			
Parameter	Unit	SA	SA	TB 1	TB 2	TB 3
R_1	$m^2.K.W^{-1}$	0.05	0.04 $\pm$0.01	0.03 $\pm$0.01	0.03 $\pm$0.01	0.03 $\pm$0.01
b_1	$J.K^{-1}.m^{-2}.s^{-1/2}$	420	471 $\pm$31	522 $\pm$50	484 $\pm$42	527 $\pm$53
$\boldsymbol{R_2}$	$\mathbf{m^2.K.W^{-1}}$	**3.12**	**3.05 $\pm$0.05**	**2.33 $\pm$0.04**	**2.13 $\pm$0.03**	**1.50 $\pm$0.01**
b_2	$J.K^{-1}.m^{-2}.s^{-1/2}$	21	38.1 $\pm$3.5	65.8 $\pm$2.2	71.7 $\pm$2.4	67.2 $\pm$4.7

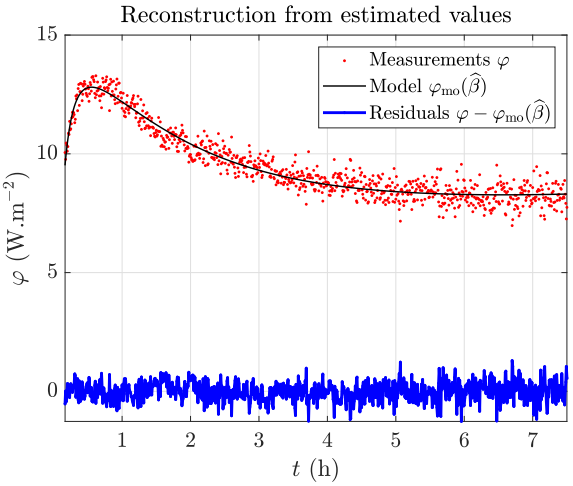

Figure 28: Comparison of measurements and model output after parameter estimation (TB 2).

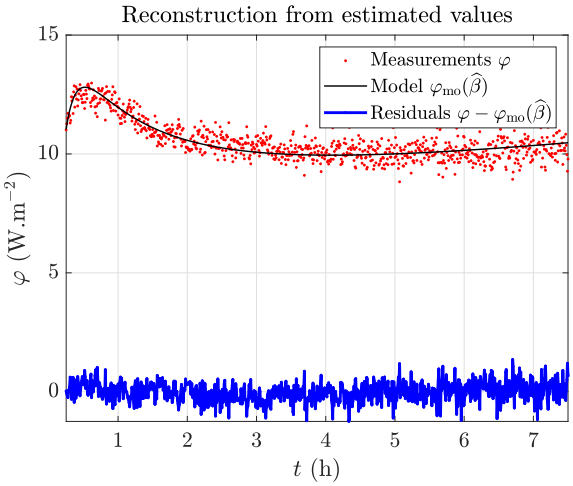

Figure 29: Comparison of measurements and model output after parameter estimation (TB 3).

ψ of this thermal bridge.

It may be noted that the uncertainties given in Tab 4 come from the V_{cor} matrix (Eq 37) of the inverse technique. Thus random measurement noise is taken into account, but measurement uncertainty of h cannot be propagated and do not contribute to the R and ψ estimation uncertainties. Therefore, the latter may be underestimated here. Bayesian inferences [73] could be advantageously used to take the uncertainty of h into account, but this is out of the scope of the present paper.

6.2 Results for different configurations

The results obtained for every active test are summarized in Tab 5. The heat transfer coefficients, equivalent thermal resistances and thermal transmittances are detailed. In every configuration (except config 6), at least four active tests are performed following the pattern shown in Fig 9. For the first test, $T_{air,e}$ is around the maximum of its sinusoid. It increases during the second test, is around its minimum during the third one, and decreases for the last test. These four regimes correspond to the four symbols $\cap$, $\nearrow$, $\cup$ and $\searrow$ used in Tab 5.

The measured heat transfer coefficient ranges between 9.1 and 10.3 with a mean value of 9.6 $W.m^{-2}.K^{-1}$. These measurements are very reproducible since the relative standard deviation between active tests is only 1%.

Thermal resistances given in Tab 5 are the sum $R_1 + R_2$ of the resistance of the first two layers of the model. For the sound area, $R_1 + R_2$ corresponds to the resistance of the thermal insulation system. For the thermal bridges, it corresponds to their equivalent resistance.

Model A was used for configurations 1 and 2 (constant external air temperature) whereas model C was preferred for other configurations (varying external air temperature). This later model requires prior quantification of the thermal properties of the building blocks layer. This was done thanks to model D (Eq 29) fed with external measurements. The estimated values are $R_3 = 0.28$ $m^2.K.W^{-1}$ and $b_3 = 703$ $J.K^{-1}.m^{-2}.s^{-1/2}$. It may be seen that despite the variations in the external temperature, the thermal resistances are estimated with a good reproducibility: the standard deviation is between 0.08 and 0.10 $m^2.K.W^{-1}$, depending on the zone considered. This corresponds to 2.6, 3.6, 5.6 and 6.3% for SA, TB 1, TB 2 and TB 3 respectively. These standard deviations are of the same magnitude of the individual estimation uncertainty predicted by the inverse method.

The thermal bridge transmission coefficients ψ, derived from these thermal resistances, are also estimated with a good reproducibility. The relative standard deviation is equal to 11% for TB 1 and TB 2 and 9% for TB 3. The individual uncertainties are of the same order of magnitude except for TB 3 for which they are smaller (about 5%). The estimated ψ-values are also in good accordance with steady-state results presented in Tab 3. Only the transmission coefficient of TB 2 is slightly over-estimated by the active method.

The results are rather independent on the magnitude of the external temperature variation. By including the external wall surface temperature T_{se} in model C, unsteady external conditions do not limit the applicability of the active method.

The presence of a temperature gradient is not a limitation either. This is an illustration of the superimposition theorem: by subtracting the initial conditions, only variations in temperature and heat flux are accounted for. This active method would therefore be applicable all year long, not only in winter time. Yet, this analysis does not consider solar gains.

7 Conclusion

This paper proposes a novel active method for the *in situ* measurement of a thermal bridge transmission coefficients ψ in a building. It is a generalization of a method originally designed for the quantification of a homogeneous wall thermal resistance. It consists in heating the indoor air with electric fan heaters for several hours. From measurements of wall surface temperatures and heat fluxes with contact sensors on a sound area (free of thermal bridge), the wall thermal resistance is estimated using an inverse technique. The latter uses a white-box 1D direct model derived from the quadrupole formalism.

This method may be used on a non-homogeneous wall (with one or several thermal bridges) by using space averages of the wall surface temperature and heat flux. This allows estimating an equivalent thermal resistance. The surface temperature and heat flux fields on the thermal bridge are measured by extrapolating contact measurements performed on a nearby sound area. The extrapolation process is based on the quantification of surface temperature differences with infrared thermography and of the total heat transfer coefficient using a "h-meter". This device uses a sinusoidal thermal load generated by thermoelectric coolers and is based on a Fourier analysis of its temperature and heat flux. This device has the main advantage of not requiring the measurement of the operative temperature.

The method is validated on a full-scale wall inside a climate chamber. This load-bearing wall is equipped with a conventional internal insulation system made of glass wool. The metallic rails which hold the insulating materials generate material-related thermal bridges. The active tests undertaken typically last 8 hours during which the indoor air temperature rises by about 15 K. The robustness of the method on the given type of wall is assessed by performing 27 active tests in 6 different configurations simulating various weather configurations (up to 15 K of external temperature variation amplitude). When the external temperature is constant, measurements on the internal surface of the wall are enough to estimate R and ψ values. When it varies however, the inverse method needs to be fed with external surface temperature measurements as well. The method showed a good repeatability and robustness to the unsteady external temperature. The measured h coefficient is estimated to about 9.6 $\mathrm{W.m^{-2}.K^{-1}}$ with only 1% standard deviation between experiments. Estimated thermal bridge linear transmittances are less than 20% away from reference values derived from steady-state measurement, and majority of them are even below 10%. The measured ψ-values range from 26 to 117 $\mathrm{mW.m^{-1}.K^{-1}}$, depending on the type of thermal bridge considered. In addition, because only variations in surface heat fluxes and temperatures are analyzed, the method is applicable whatever the external temperature mean value. It may be either above or below the internal temperature.

The method has the advantage of being almost non-intrusive: very few contact sensors are needed and they are not placed on thermal bridges but on a nearby zone. However, this method has several limitations. First, a sound area is required on the wall to fix a HFM: surface heat fluxes are extrapolated from this reference. If the distance between thermal bridges is not sufficient for the heat transfer to be 1D at least on one location of the wall, no reference heat flux contact measurement is possible. Second, this method is not applicable for external insulation systems. Indeed, the thermal load must take place on the side of the insulation layers to maximize sensitivity to the desired thermal resistance and to avoid lateral losses.

Future work will consist in validating the method *in situ* (field measurements) and on other types of wall. This study focused on a load bearing internally insulated wall with linear thermal bridges. The authors do not anticipate any difficulty to apply the same technique to lightweight walls. They do not foresee any complication either for the characterization of point thermal bridges. In addition, Bayesian inferences could be used in the parameter estimation (inverse method) for a better quantification of estimation uncertainties. In particular, this would enable a better propagation of the measurement uncertainty over the total heat transfer coefficient.

Acknowledgments

The authors would like to thank Etienne Hombourger, Heidi Kauffmann, Arnaud Escal and Laurent Peiffer at CEREMA-DterEst of Nancy for making available their climate chamber for our experimental campaign. They also would like to thank ANRT (Association Nationale de la Recherche et de la Technologie) for its financial support (CIFRE grant number 2017/1263).

References

References

[1] L. Gynther, B. Lappillone, and K. Pollier. Energy efficiency trends and policies in the household and tertiary sectors. *An analysis based on the ODYSSEE and MURE databases*, 2015.

[2] A. Stafford, M. Bell, and C. Gorse. Building Confidence – A working paper. Report 008, The Centre for Low Carbon Futures, March 2012.

[3] D. Johnston, D. Miles-Shenton, and D. Farmer. Quantifying the domestic building fabric 'performance gap'. *Building Services Engineering Research and Technology*, 36(5):614–27, 2015.

[4] P. De Wilde. The gap between predicted and measured energy performance of buildings: A framework for investigation. *Automation in Construction*, 41:40–49, 2014.

[5] A.C. Menezes, A. Cripps, D. Bouchlaghem, and R. Buswell. Predicted vs. actual energy performance of non-domestic buildings: Using post-occupancy evaluation data to reduce the performance gap. *Applied energy*, 97:355–364, 2012.

[6] S. Farkh. Les ponts thermiques dans le bâtiment – Mieux les connaître pour mieux les traiter. Technical report, Centre Scientifique et Technique du Bâtiment (CSTB), 2014, (in French).

[7] T.G. Theodosiou and A.M. Papadopoulos. The impact of thermal bridges on the energy demand of buildings with double brick wall constructions. *Energy and Buildings*, 40(0):2083–2089, 2008.

Table 5: Estimations of thermal resistance and thermal bridge transmission coefficient for every experiment. Depending on the experiment, $T_{air,e}$ is constant: $-$, or around a maximum: $\cap$, or increasing: $\nearrow$, or around a minimum: $\cup$, or decreasing: $\searrow$.

Conf	Exp	$T_{air,e}$	h $(W.m^{-2}.K^{-1})$	$R_1 + R_2$ $(m^2.K.W^{-1})$				ψ $(mW.m^{-1}.K^{-1})$		
				SA	TB 1	TB 2	TB 3	TB 1	TB 2	TB 3
1	1	$-$	10.1 ±0.6	3.09 ±0.14	2.20 ±0.10	1.97 ±0.08	1.45 ±0.03	29 ±6	41 ±6	114 ±7
	2	$-$	9.7 ±0.6	3.07 ±0.07	2.28 ±0.05	2.13 ±0.05	1.54 ±0.03	25 ±3	32 ±3	100 ±5
	3	$-$	9.7 ±0.7	3.16 ±0.11	2.33 ±0.08	2.11 ±0.06	1.55 ±0.03	27 ±4	38 ±4	110 ±6
	4	$-$	9.6 ±0.4	3.14 ±0.20	2.36 ±0.17	2.20 ±0.16	1.60 ±0.04	25 ±8	32 ±9	102 ±9
	5	$-$	10.3 ±0.8	3.07 ±0.08	2.20 ±0.05	2.01 ±0.04	1.49 ±0.02	29 ±3	39 ±3	107 ±5
2	6	$-$	9.6 ±0.4	3.06 ±0.11	2.29 ±0.09	2.24 ±0.09	1.51 ±0.03	24 ±5	27 ±5	104 ±6
	7	$-$	9.6 ±0.5	3.16 ±0.07	2.40 ±0.05	2.31 ±0.05	1.55 ±0.02	24 ±3	28 ±3	110 ±4
	8	$-$	9.5 ±0.4	3.09 ±0.06	2.36 ±0.04	2.28 ±0.04	1.53 ±0.02	23 ±2	27 ±3	105 ±4
3	9	$\cap$	9.4 ±0.5	3.02 ±0.12	2.18 ±0.09	2.07 ±0.08	1.41 ±0.03	27 ±5	33 ±5	110 ±6
	10	$\nearrow$	9.9 ±0.5	3.05 ±0.12	2.21 ±0.09	2.07 ±0.08	1.38 ±0.03	27 ±5	34 ±5	117 ±6
	11	$\cup$	9.5 ±0.5	3.04 ±0.14	2.18 ±0.10	2.00 ±0.09	1.36 ±0.04	28 ±6	37 ±6	119 ±8
	12	$\searrow$	9.6 ±0.3	3.05 ±0.07	2.24 ±0.05	2.07 ±0.04	1.40 ±0.02	26 ±3	34 ±3	115 ±4
4	13	$\cap$	9.5 ±0.4	2.92 ±0.14	2.11 ±0.11	1.91 ±0.09	1.35 ±0.04	26 ±6	36 ±6	106 ±8
	14	$\nearrow$	9.5 ±0.4	3.05 ±0.13	2.23 ±0.10	2.02 ±0.08	1.33 ±0.03	26 ±5	37 ±5	124 ±7
	15	$\cup$	9.3 ±0.4	3.24 ±0.10	2.41 ±0.09	2.21 ±0.07	1.47 ±0.04	27 ±5	37 ±5	132 ±7
	16	$\searrow$	9.8 ±0.5	2.97 ±0.08	2.18 ±0.06	2.04 ±0.06	1.41 ±0.02	25 ±3	32 ±4	105 ±5
5	17	$\cap$	10.3 ±0.8	3.13 ±0.16	2.16 ±0.10	2.02 ±0.10	1.34 ±0.05	33 ±6	41 ±7	134 ±9
	18	$\cap$	9.5 ±0.5	3.21 ±0.16	2.28 ±0.12	2.12 ±0.10	1.42 ±0.04	31 ±6	40 ±7	135 ±9
	19	$\nearrow$	9.7 ±0.6	3.09 ±0.16	2.25 ±0.11	2.11 ±0.12	1.55 ±0.04	27 ±6	34 ±6	102 ±7
	20	$\nearrow$	9.3 ±0.5	2.96 ±0.12	2.19 ±0.09	2.05 ±0.08	1.33 ±0.04	24 ±5	31 ±5	113 ±7
	21	$\cup$	9.7 ±0.7	3.01 ±0.08	2.27 ±0.06	2.12 ±0.05	1.45 ±0.03	23 ±3	30 ±3	104 ±5
	22	$\cup$	9.0 ±0.5	2.99 ±0.06	2.19 ±0.04	2.04 ±0.04	1.40 ±0.02	26 ±3	33 ±3	108 ±4
	23	$\searrow$	9.6 ±0.4	3.09 ±0.08	2.26 ±0.06	2.14 ±0.05	1.50 ±0.03	27 ±3	33 ±3	108 ±5
	24	$\searrow$	9.1 ±0.5	3.00 ±0.06	2.12 ±0.04	1.98 ±0.04	1.38 ±0.02	29 ±3	36 ±3	112 ±4
6	25	$\cap$	9.6 ±0.4	2.99 ±0.13	2.19 ±0.10	2.05 ±0.08	1.29 ±0.03	26 ±5	32 ±5	123 ±7
	26	$\nearrow$	9.6 ±0.5	3.00 ±0.15	2.29 ±0.12	2.17 ±0.11	1.28 ±0.04	22 ±6	27 ±6	124 ±8
	27	$\searrow$	9.5 ±0.4	2.92 ±0.08	2.17 ±0.06	2.13 ±0.05	1.44 ±0.03	24 ±3	25 ±3	95 ±5
average			9.6	3.05	2.24	2.09	1.43	26	34	112
standard deviation			0.1	0.08	0.08	0.10	0.09	3	4	10

[8] G. Evola, G. Margani, and L. Marletta. Energy and cost evaluation of thermal bridge correction in Mediterranean climate. *Energy and Buildings*, 43(9):2385–2393, 2011.

[9] A.B. Larbi. Statistical modelling of heat transfer for thermal bridges of buildings. *Energy and Buildings*, 37(0):945–951, 2005.

[10] SAP BRE. The Government's Standard Assessment Procedure for Energy Rating of Dwellings. Technical Report version 9.92, Building Research Establishment (BRE), Watford, UK, Watford, UK, October 2012.

[11] ISO 14683:2007. Thermal bridges in building construction - Linear thermal transmittance - Simplified methods and default values. *International Standards Organisation*, 2007.

[12] ISO 10211:2017. Thermal bridges in building construction - Heat flows and surface temperatures - Detailed calculations. *International Standards Organisation*, (14683), 2017.

[13] A. François, L Ibos., V. Feuillet, and J. Meulemans. Estimation of the thermal resistance of a building wall with inverse techniques based on rapid in situ measurements and white-box or ARX black-box models. *Energy and Buildings*, 226:110346, 2020.

[14] A. François, L. Ibos, V. Feuillet, and J. Meulemans. Novel in situ measurement methods of the total heat transfer coefficient on building walls. *Energy and Buildings*, 219:110004, 2020.

[15] ISO 13187:1999. Thermal Performance of Buildings - Qualitative Detection of Thermal Irregularities in Building Envelopes - Infrared method (ISO 6781:1983 Modified). *International Standards Organisation*, 1999.

[16] C.A. Balaras and A.A. Argiriou. Infrared thermography for building diagnostics. *Energy and Buildings*, 34(2):171–83, 2002.

[17] A. Kylili, P.A. Fokaides, P. Christou, and S.A. Kalogirou. Infrared thermography (IRT) applications for building diagnostics: A review . *Applied Energy*, 134(0):531–49, 2014.

[18] I. Nardi, E. Lucchi, T. de Rubeis, and D. Ambrosini. Quantification of heat energy losses through the building envelope: A state-of-the-art analysis with critical and comprehensive review on infrared thermography. *Building and Environment*, 2018.

[19] D. Pajani. *La thermographie du bâtiment – Principes et applications du diagnostic thermographique*. Eyrolles, 2012, (in French).

[20] F. Asdrubali, G. Baldinelli, F. Bianchi, D. Costarelli, A. Rotili, M. Seracini, and G. Vinti. Detection of thermal bridges from thermographic images by means of image processing approximation algorithms. *Applied Mathematics and Computation*, 317:160–171, 2018.

[21] I. Garrido, S. Lagüela, T. Arias, and J. Balado. Thermal-based analysis for the automatic detection and characterization of thermal bridges in buildings. *Energy and Buildings*, 158:1358–1367, 2018.

[22] E. Grinzato, V. Vavilov, and T. Kauppinen. Quantitative infrared thermography in buildings. *Energy and Buildings*, 29(1):1–9, 1998.

[23] K. Kurita, M. Oyado, H. Tanaka, and S. Tottori. Active infrared thermographic inspection technique for elevated concrete structures using remote heating system. *Infrared Physics & Technology*, 52(5):208–213, 2009.

[24] C. Maierhofer, R. Arndt, M. Röllig, C. Rieck, A. Walther, H. Scheel, and B. Hillemeier. Application of impulse-thermography for non-destructive assessment of concrete structures. *Cement and Concrete Composites*, 28(4):393–401, 2006.

[25] T. Taylor, J. Counsell, S. Gill, and G. Oakley. Assessing the severity of workmanshipdefects using thermography and 2-d and 3-d heat transfer models. In *Proc. of Sustainable Building Conference (SB13)*, Graz (Austria), September 2013.

[26] P.G. Bison, M.D. Bardeschi, E. G Grinzato, T. T Kauppinen, E. Rosina, and G. Tucci. Survey of facades based on thermal scanning: Palazzo della Ragione, Milan, Italy. In *Thermosense XVIII: An International Conference on Thermal Sensing and Imaging Diagnostic Applications*, volume 2766, pages 55–64. International Society for Optics and Photonics, 1996.

[27] Z. Li, W. Yao, S. Lee, C. Lee, and Z. Yang. Application of infrared thermography technique in building finish evaluation. *Journal of Nondestructive Evaluation*, 19(1):11–19, 2000.

[28] S.S. de Freitas, V.P. de Freitas, and E. Barreira. Detection of façade plaster detachments using infrared thermography–A nondestructive technique. *Construction and Building Materials*, 70:80–87, 2014.

[29] J. Laranjeira, N. Simões, I. Simões, A. Tadeu, and C. Serra. Passive thermography evaluation of bonding defects in adhered ceramic tiling: experimental and in-situ assessments. In *12th International Conference on Quantitative InfraRed Thermography (QIRT 2014)*, Bordeaux, France, July 7-11 2014.

[30] C. Ibarra-Castanedo, S. Sfarra, M. Klein, and X. Maldague. Solar loading thermography: Time-lapsed thermographic survey and advanced thermographic signal processing for the inspection of civil engineering and cultural heritage structures. *Infrared Physics & Technology*, 82:56–74, 2017.

[31] R. Douguet, T.T. Ha, V. Feuillet, J. Meulemans, and L. Ibos. A novel experimental method for the in situ detection of thermal bridges in building envelopes based on active infrared thermography and singular value decomposition analysis. *The 14th Quantitative InfraRed Thermography Conference*, Berlin, Germany, 25 to 29 June 2018.

[32] K. Martin, C. Escudero, A. Erkoreka, I. Flores, and J.M. Sala. Equivalent wall method for dynamic characterisation of thermal bridges. *Energy and Buildings*, 55(0):704–14, 2012.

[33] E. Kossecka and J. Kosny. Equivalent wall as a dynamic model of a complex thermal structure. *Journal of Thermal Insulation and Building Envelopes*, 20(3):249–268, 1997.

[34] J. Quinten and V. Feldheim. Dynamic modelling of multidimensional thermal bridges in building envelopes: Review of existing methods, application and new mixed method. *Energy and Buildings*, 110:284–93, 2016.

[35] J. Quinten and V. Feldheim. Mixed equivalent wall method for dynamic modelling of thermal bridges: Application to 2-D details of building envelope. *Energy and Buildings*, 183:697–712, 2019.

[36] F. Aguilar, J.P. Solano, and P.G. Vicente. Transient modeling of high-inertial thermal bridges in buildings using the equivalent thermal wall method. *Applied thermal engineering*, 67(1-2):370–377, 2014.

[37] A. Nagata. A simple method to incorporate thermal bridge effects into dynamic heat load calculation programs. In *International IBPSA Conference*, pages 817–822, 2005.

[38] X. Xiaona and J. Yi. Equivalent slabs approach to simulate the thermal performance of thermal bridges in building constructions. *IBPSA, Proceedings Building Simulation*, pages 287–293, 2007.

[39] T. Taylor, J. Counsell, and S. Gill. Combining thermography and computer simulation to identify and assess insulation defects in the construction of building façades. *Energy and Buildings*, 76:130–142, 2014.

[40] E. Cuce and P.M. Cuce. The impact of internal aerogel retrofitting on the thermal bridges of residential buildings: An experimental and statistical research. *Energy and Buildings*, 116:449–54, 2016.

[41] A. Aïssani, A. Chateauneuf, J.-P. Fontaine, and Ph. Audebert. Quantification of workmanship insulation defects and their impact on the thermal performance of building facades. *Applied Energy*, 165:272–84, 2016.

[42] H. Heinrich and K. Dahlem. Thermography of low energy buildings. In *Proc. of International Conference on Quantitative InfraRed Thermography (QIRT 2000)*, Reims (France), July 2008.

[43] L. Zalewski, S. Lassue, D. Rousse, and K. Boukhalfa. Experimental and numerical characterization of thermal bridges in prefabricated building walls. *Energy Conversion and Management*, 51(12):2869–77, 2010.

[44] F. Ascione, N. Bianco, R.F. De Masi, F. de'Rossi, and G.P. Vanoli. Simplified state space representation for evaluating thermal bridges in building: Modelling, application and validation of a methodology. *Applied Thermal Engineering*, 61(2):344–354, 2013.

[45] F. Ascione, N. Bianco, R.F. De Masi, G. M. Mauro, M. Musto, and G.P. Vanoli. Experimental validation of a numerical code by thin film heat flux sensors for the resolution of thermal bridges in dynamic conditions. *Applied Energy*, 124:213–22, 2014.

[46] A. Wrobel and T. Kisilewicz. Detection of thermal bridges - aims, possibilities and conditions. In *Proc. of 9th International Conference on Quantitative InfraRed Thermography (QIRT 2008)*, Krakow (Poland), July 2008.

[47] C. Serra, A. Tadeu, N. Simões, and I. Simões. Simulation of heat diffusion in multi-layered construction systems for active IRT data analysis. In *Proc. of 12th International Conference on Quantitative InfraRed Thermography (QIRT 2014)*, Bordeaux (France), July 2014.

[48] K. Martin, A. Campos-Celador, C. Escudero, I. Gomez, and J.M. Sala. Analysis of a thermal bridge in a guarded hot box testing facility. *Energy and Buildings*, 50:139–49, 2012.

[49] ISO 8990:1996. Thermal insulation – Determination of steady-state thermal transmission properties – Calibrated and guarded hot box. *International Standards Organisation*, 1996.

[50] M. O'Grady, A.A. Lechowska, and A.M. Harte. Infrared thermography technique as an in-situ method of assessing heat loss through thermal bridging. *Energy and Buildings*, 135:20–32, 2017.

[51] M. O'Grady, A. A Lechowska, and A. M Harte. Quantification of heat losses through building envelope thermal bridges influenced by wind velocity using the outdoor infrared thermography technique. *Applied energy*, 208:1038–1052, 2017.

[52] F. Asdrubali, G. Baldinelli, and F. Bianchi. A quantitative methodology to evaluate thermal bridges in buildings. *Applied Energy*, 97(0):365–73, 2012.

[53] G. Baldinelli, F. Bianchi, A. Rotili, D. Costarelli, M. Seracini, G. Vinti, F. Asdrubali, and L. Evangelisti. A model for the improvement of thermal bridges quantitative assesment by infrared thermography. *Applied Energy*, 211:854–864, 2018.

[54] T.I Ward. *Assessing the effects of thermal bridging at junctions and around openings*. Number 1. 2006.

[55] I. Benko. Quantitative analysis of thermal bridges of structures through infrared thermographs. In *6th International Conference on Quantitative InfraRed Thermography (QIRT 2002)*, Dubrovnik (Croatia), September 2002.

[56] F. Bianchi, A.L. Pisello, G. Baldinelli, and F. Asdrubali. Infrared Thermography Assessment of Thermal Bridges in Building Envelope: Experimental Validation in a Test Room Setup. *Sustainability*, 6(10):7107, 2014.

[57] I. Nardi, D. Ambrosini, D. Paoletti, and S. Sfarra. Combining Infrared Thermography and Numerical Analysis for Evaluating Thermal Bridges In Buildings: A Case Study. *International Journal of Engineering Research and Applications*, 5(1):67–76, 2015.

[58] A. François, L. Ibos, V. Feuillet, and J. Meulemans. Building thermal bridge heat losses quantification by infrared thermography. Steady-state evaluation and uncertainty calculation. In *Journal of Physics: Conference Series*, volume 1343, page 012171. IOP Publishing, 2019.

[59] H. Preston-Thomas. The international temperature scale of 1990 (ITS-90). *Metrologia*, 27(1):3, 1990.

[60] S. Datcu, L. Ibos, Y. Candau, and S. Matteï. Improvement of building wall surface temperature measurements by infrared thermography. *Infrared physics & technology*, 46(6):451–467, 2005.

[61] ISO 9869-1:2014. Thermal insulation – Building elements – In-situ measurement of thermal resistance and thermal transmittance – Part 1: Heat flow meter method. *International Standards Organisation*, 2014.

[62] ISO 6946:2017. Building components and building elements - Thermal resistance and thermal transmittance - Calculation methods. *International Standards Organisation*, 2017.

[63] IEC ISO and BIPM OIML. Guide to the Expression of Uncertainty in Measurement. *Geneva, Switzerland*, 122, 1995.

[64] D. Maillet, S. André, J.C. Batsale, A. Degiovanni, and C. Moyne. *Thermal quadrupoles: solving the heat equation through integral transforms*. John Wiley & Sons Inc, 2000.

[65] F.R. De Hoog, J.H. Knight, and A.N. Stokes. An improved method for numerical inversion of Laplace transforms. *SIAM Journal on Scientific and Statistical Computing*, 3(3):357–366, 1982.

[66] K. Levenberg. A method for the solution of certain non-linear problems in least squares. *Quarterly of Applied Mathematics*, 2(2):164–168, 1944.

[67] D.W. Marquardt. An algorithm for least-squares estimation of nonlinear parameters. *Journal of the society for Industrial and Applied Mathematics*, 11(2):431–441, 1963.

[68] J.J. Moré. The Levenberg-Marquardt algorithm: implementation and theory. In *Numerical analysis*, pages 105–116. Springer, 1978.

[69] J.V Beck, B. Blackwell, and C. R St Clair Jr. *Inverse heat conduction: Ill-posed problems*. Wiley Interscience, 1985.

[70] S.E. Gustafsson. Transient plane source techniques for thermal conductivity and thermal diffusivity measurements of solid materials. *Review of scientific instruments*, 62(3):797–804, 1991.

[71] J.C. Jones and M. Wade. On the thermal diffusivity of insulating glass wool. *Journal of fire sciences*, 18(1):74–77, 2000.

[72] A. François, L. Ibos, V. Feuillet, and J. Meulemans. In situ measurement of the heat transfer coefficient on a building wall surface: h-measurement device based on a harmonic excitation. *Entropie*, 2020.

[73] J.V. Beck and K.J. Arnold. *Parameter Estimation in Engineering and Science*. Wiley Interscience, 1977.

A Details on h-measurement method

The operative temperature T_{op} is supposed to be constant for several oscillation periods. The mean values of the temperature and heat flux over these few periods are subtracted. Let denote T_h and φ_h these zero-mean quantities. In the frequency domain, Eq 39 becomes:

$$\underline{\varphi_h} = h\underline{T_h} \tag{42}$$

where lower bars denote complex harmonic quantities. The heat transfer coefficient is simply given by:

$$h = \Re\left(\frac{\varphi_h}{T_h}\right) = \frac{\mathcal{A}_\varphi}{\mathcal{A}_T}\cos\left(\zeta\right) \tag{43}$$

with $\Re$ the real part operator, $\mathcal{A}_\varphi$ and $\mathcal{A}_T$ the amplitudes of φ_h and T_h, and ζ the phase lag between them. In practice, the h-value is derived from the discrete Fourier transforms FT_T and FT_φ of the signals:

$$h = \Re\left(\frac{FT_\varphi\left(k_f\right)}{FT_T\left(k_f\right)}\right) \tag{44}$$

with k_f the index of the harmonic corresponding to the excitation frequency f. It may be shown that the measurement uncertainty is given by:

$$\mathrm{u}\left(h\right) = \frac{1}{\mathcal{A}_T}\sqrt{\mathrm{u}^2\left(A_\varphi\right) + \left(\frac{\mathcal{A}_\varphi}{\mathcal{A}_T}\right)^2 \mathrm{u}^2\left(A_\varphi\right)} \tag{45}$$

This method and its optimization are presented in further details in [72]. The best operating conditions of the device were identified. First, the oscillation frequency f has to be high enough for T_{op} to be considered constant during several periods but low enough for the period to be larger than the HFM response time. A period of 5 min proved to be a good optimum. Second, the amplitude of the oscillations cannot be too small (for the signal-to-noise ratio to be high enough) neither too large (a significant temperature increase would change the convective pattern of the air flow and introduce a bias in the measurement). An optimum value was also found: the power supplied to the TECs was set such that the temperature oscillation amplitude was close to 0.3 K.